Insights for the melt migration, the volcanic activity and the ultrafast lithosphere delamination related to the Yellowstone plume (Western USA)

A. Rigo, C. Adam, M. Grégoire, M. Gerbault, R. Meyer, M. Rabinowicz, F. Fontaine, S. Bonvalot

Geophysical Journal International

Geophys. J. Int. (2015) **203,** 1274–1301 doi: 10.1093/gji/ggv360
GJI Geodynamics and tectonics

Insights for the melt migration, the volcanic activity and the ultrafast lithosphere delamination related to the Yellowstone plume (Western USA)

A. Rigo,[1] C. Adam,[2] M. Grégoire,[3] M. Gerbault,[3] R. Meyer,[4] M. Rabinowicz,[3] F. Fontaine[5] and S. Bonvalot[3]

[1]*Laboratoire de Géologie, École Normale Supérieure, CNRS, PSL Research University, 24 rue Lhomond, F*75231 *Paris Cedex 5, France. E-mail: alexis.rigo@ens.fr*
[2]*Virginia Tech., Geosciences Department, Blacksburg, VA, USA*
[3]*Géosciences Environnement Toulouse - CNRS, IRD, Université de Toulouse, Observatoire Midi-Pyrénées, F*-31400 *Toulouse, France*
[4]*Centre for Geobiology and Department for Earth Sciences, University of Bergen,* 5007 *Bergen, Norway*
[5]*Institut de Physique du Globe de Paris, Observatoire Volcanologique du Piton de la Fournaise, Île de la Réunion, France*

Accepted 2015 August 25. Received 2015 August 25; in original form 2015 February 13

SUMMARY

The Yellowstone–East Snake River Plain hotspot track has been intensely studied since several decades and is widely considered to result from the interaction of a mantle plume with the North American plate. An integrated conclusive geodynamic interpretation of this extensive data set is however presently still lacking, and our knowledge of the dynamical processes beneath Yellowstone is patchy. It has been argued that the Yellowstone plume has delaminated the lower part of the thick Wyoming cratonic lithosphere. We derive an original dynamic model to quantify delamination processes related to mantle plume–lithosphere interactions. We show that fast (∼300 ka) lithospheric delamination is consistent with the observed timing of formation of successive volcanic centres along the Yellowstone hotspot track and requires (i) a tensile stress regime within the whole lithosphere exceeding its failure threshold, (ii) a purely plastic rheology in the lithosphere when stresses reach this yield limit, (iii) a dense lower part of the 200 km thick Wyoming lithosphere and (iv) a decoupling melt horizon inside the median part of the lithosphere. We demonstrate that all these conditions are verified and that ∼150 km large and ∼100 km thick lithospheric blocks delaminate within 300 ka when the Yellowstone plume ponded below the 200 km thick Wyoming cratonic lithosphere. Furthermore, we take advantage of the available extensive regional geophysical and geological observation data sets to design a numerical 3-D upper-mantle convective model. We propose a map of the ascending convective sheets contouring the Yellowstone plume. The model further evidences the development of a counter-flow within the lower part of the lithosphere centred just above the Yellowstone mantle plume axis. This counter-flow controls the local lithospheric stress field, and as a result the trajectories of feeder dykes linking the partial melting source within the core of the mantle plume with the crust by crosscutting the lithospheric mantle. This counter-flow further explains the 50 km NE shift observed between the mantle plume axis and the present-day Yellowstone Caldera as well as the peculiar shaped crustal magma chambers.

Key words: Instability analysis; Mantle processes; Cratons; Dynamics: convection currents, and mantle plumes; Hotspots; North America.

1 INTRODUCTION

The Earth's mantle plumes, or hotspots, can be divided into three categories based on various criteria including seismic tomography, topography, geodesy, geochronology and tectonics as proposed by Courtillot *et al.* (2003): (i) mantle plumes having the deepest origin at the core–mantle boundary, called 'primary' plumes, such as those from Hawaii, La Réunion and Iceland; (ii) mantle plumes originating at the mantle transition zone above associated superswells (e.g. Pacific and Africa), called 'secondary' plumes such as those of Tahiti, Pitcairn and Hoggar; and (iii) mantle plumes restricted to the upper mantle induced by lithospheric breakup and extension. The latter are no mantle plumes in *sensu stricto*.

The existence of a plume at Yellowstone is still debated and some authors proposed alternative models such as melting due to slab fragmentation and trench retreat (James *et al.* 2011). However,

the plume hypothesis is supported by several strong arguments. Hotspot/plume volcanism is characterized by the development of a 'hotspot track', that is, the focusing in time and space of volcanic activity, producing a distribution of oriented successive 'isolated' volcanic centres as the plate moves above the mantle plume. Such a hotspot track has been described for the Yellowstone–Snake River Plain (YSRP) volcanic province (e.g. Shervais & Hanan 2008; Pierce & Morgan 2009; Smith *et al.* 2009; Kincaid *et al.* 2013). Based on thermal considerations, Pierce & Morgan (2009) suggested that the 'Yellowstone plume' is deeply rooted at the core–mantle boundary even if they have no tomographic evidence for such a setting. Nonetheless, this hypothesis and the 'primary' plume characteristics are further supported by the Columbia River flood basalt (e.g. Camp 1995) in addition to the hotspot track (Courtillot *et al.* 2003).

However, the 'standard' plume model alone cannot account for the mechanisms of initiation and development of voluminous flood basalt and of hotspot tracks, particularly in a thick cratonic lithosphere context (King & Anderson 1995). In the case of Yellowstone, the fast progression (<1 Ma) of the successive volcanic centres along the hotspot track through the Wyoming cratonic lithosphere remains enigmatic. Several authors proposed that the lithosphere could be eroded and then delaminated by instabilities developing at its base and driven by density contrasts (Houseman & McKenzie 1981, 1982; Fourel *et al.* 2013; Molnar & Houseman 2013; Johnson *et al.* 2014). These instabilities would be favoured by the long history of the cratonic lithosphere starting in Archean times. Such an old craton encountered different cycles of rejuvenation/refertilization events related to magmatic underplating and melt depletion events (Carlson *et al.* 2004; Foley 2008; Thybo & Artemieva 2013). One consequence is the formation of a stratified lithosphere with dense and buoyant layers, which also influences its internal stress field and its response to extension (Liao *et al.* 2013).

In the present study, after specifying the geological and geodynamical contexts of Western USA (Section 2), we first focus on the timing of the delamination process (Section 3). The timing of formation of volcanic centres along the Yellowstone hotspot track requires recent and nearly instantaneous erosion of the lower Wyoming lithosphere by the mantle plume. Using a stability analysis, we show that such a fast delamination is possible when taking into account four specific conditions: (i) a tensile stress within the whole lithosphere exceeding up to its yield limit, (ii) a purely plastic rheology for the lithosphere where stresses reach this failure threshold, (iii) a dense lower part of the 200-km thick Wyoming lithosphere and (iv) a decoupling melt horizon occurring inside the median part of the lithosphere. We also interpret the high-resolution tomographic images resulting from the deployment of the USArray seismic network to infer that they are consistent with the existence of a secondary type mantle plume (Courtillot *et al.* 2003) developing at the mantle transition zone. Accordingly, we develop an original 3-D numerical model of the Yellowstone mantle plume (Section 4). Primary model predictions are challenged with geological and geophysical observations (Section 5) and we provide our conclusions in Section 6.

2 GEODYNAMICAL CONTEXT OF THE WESTERN USA

2.1 Geological setting

The present-day lithosphere below the YSRP volcanic region results from a geological history beginning in the Archean (3.6–3.0 Ga) by the formation of the Wyoming craton (Fig. 1). The geological craton evolution has been marked by magmatism and tectonism in late Archean times followed by rifting and mafic underplating during Proterozoic times (Chamberlain *et al.* 2003). A long period of tectonic quiescence prevailed between ∼2.7 Ga and ∼150 Ma. Geodynamic processes restarted when the subduction of the Farallon plate began to the west. During the Sevier-Laramide orogeny (140–45 Ma), the flat subduction beneath the Wyoming craton resulted not only in crustal shortening but caused also lithospheric hydration, metasomatism and magmatic underplating (Livaccari & Perry 1993; English *et al.* 2003; DeCelles 2004; Kusky *et al.* 2014). Finally, the present-day regional stress field is dominated by the subduction of the Juan de Fuca slab beneath Cascadia, which interacts with the western North American plate.

During the Neogene, the emplacement of the worldwide youngest Large Igneous Province started a new geodynamical active phase in the area of interest. The Columbia River Basalts erupted 17 Ma ago and were followed by the formation of the silicic centres of the High Lava Plains (HLP). Then, the YSRP erupted following an SW–NE trend parallel to the North American plate motion (Pierce & Morgan 1992, 2009). The YSRP contains a worldwide unique succession of giant calderas with a volcanic age progression from 16.5 to 0.63 Ma, the latter corresponding to the last eruption of the active caldera located in Yellowstone Park (Figs 1 and 5). The origin of this hotspot track, doubled by a less active branch along the HLP, is still controversial. The most popular interpretation is the presence of a rising mantle plume interacting with the lithosphere. In this scenario, the successive calderas are generated through the motion of the American plate at a velocity *ca.* 2.5 cm yr^{-1} in the SW direction (e.g. Pierce & Morgan 1992, 2009; Shervais & Hanan 2008; DeNosaquo *et al.* 2009; Smith *et al.* 2009; Jean *et al.* 2014; Obrebski *et al.* 2011). Moreover, Kincaid *et al.* (2013) proposed that the double track is caused by a bifurcation of the plume head due to its interaction with the western subducting slab. Alternatively, the interaction between the mantle and the subducting slab is also proposed to have formed the Yellowstone track without the presence of a mantle plume. In such case, the origin of volcanism is explained by fragmentation of the Farallon slab (James *et al.* 2011) or by local convection in the upper mantle with magma production within the lithosphere to account for a not so hot volcanism (Humphreys *et al.* 2000; Foulger & Natland 2003; Leeman *et al.* 2009).

One key question underlying this controversy is the evolution of the thickness and of the composition of the crust and of the lithospheric mantle. A thick crust with underplated and intruded mafic to ultramafic lithology seems to clearly characterize the YSRP and the Wyoming craton regions (e.g. DeNosaquo *et al.* 2009). Several studies of mantle xenoliths have shown that subcontinental lithospheric mantle (SCLM) is generally depleted due to the extraction of mafic melts throughout the geological history (Carlson *et al.* 2004; Griffin *et al.* 2004; Tang *et al.* 2013 and references therein). Such a depleted cratonic lithosphere is buoyant and should not be easily delaminated by asthenospheric convection. Nevertheless, there are evidences indicating that cratonic lithosphere such as the one underlying the YSRP - Wyoming province has been refertilized by magma ascents and associated metasomatism (Griffin *et al.* 2004; O'Reilly & Griffin 2010; Tang *et al.* 2013). This refertilization would have acted early during the meso-Proterozoic and was probably enhanced by active extension. The intrusion and subsequent crystallization of mafic veins, dykes and sills significantly increase the lithospheric density, which thickens by the accumulation of resulting meta-basaltic eclogites. Such a refertilized lithospheric mantle can thus be more easily delaminated. Furthermore, this process

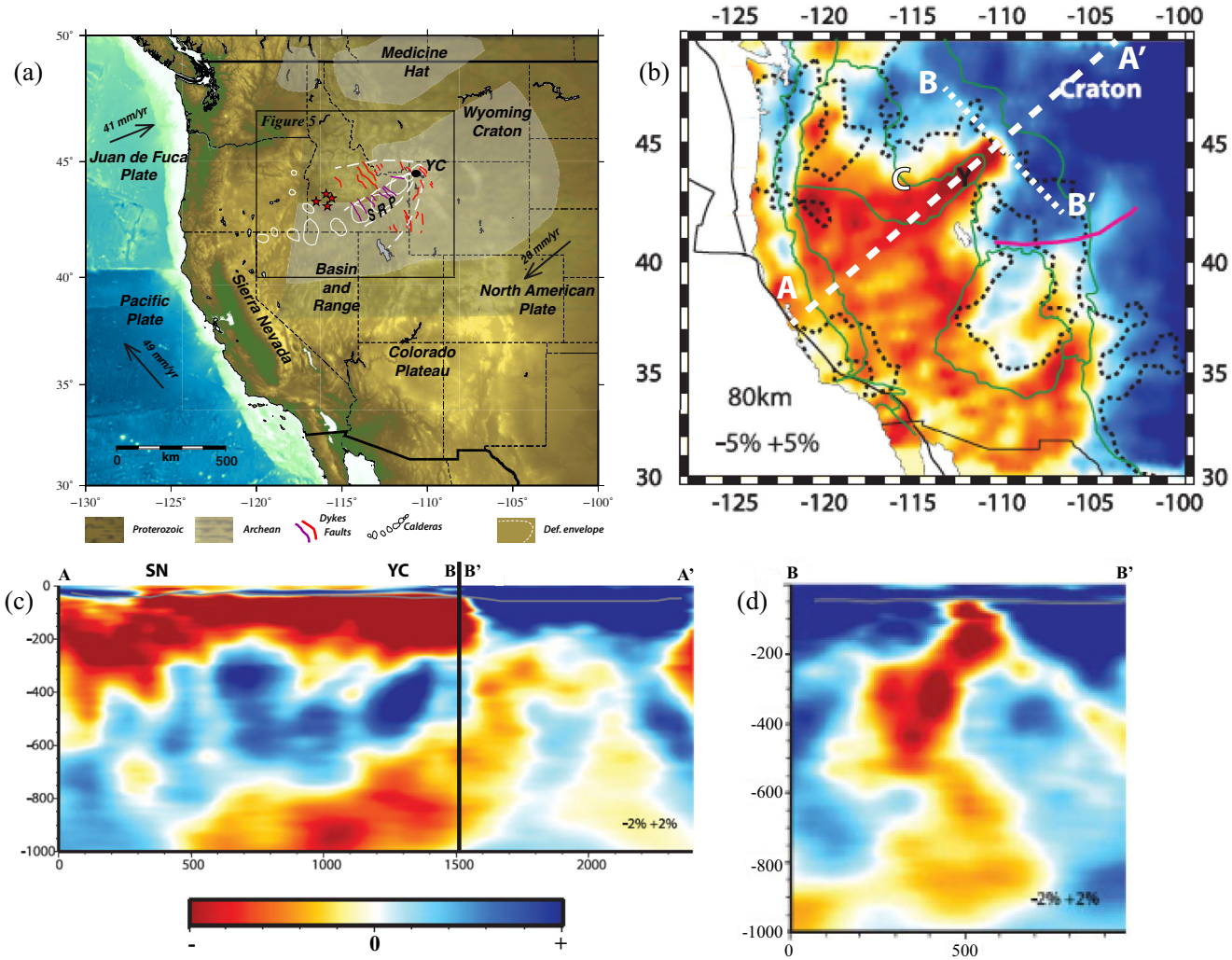

Figure 1. Geodynamic of western USA. (a) Tectonic map. In grey the Archean cratons of Wyoming and Medicine Hat from Foster *et al.* (2006). The dykes in the Snake River Plain and the Pleistocene–Quaternary major faults are indicated in violet and in red, respectively (modified from Kuntz *et al.* 1992; Pierce & Morgan 1992; Parsons *et al.* 1998). The present-day deformation V-shaped envelope, also called tectonic parabola, is drawn in white with the successive calderas along the hotspot track of Yellowstone plume (from Pierce & Morgan 1992; Shervais & Hanan 2008; DeNosaquo *et al.* 2009; Smith *et al.* 2009); red stars locate the most recent activity (−1.8 to −0.8 Ma) of high-K alkali basalts and low-K tholeiitic basalts from Shervais & Vetter (2009); SRP: Snake River Plain; YC: Yellowstone Caldera; the absolute plate motions are also indicated. (b) Map of the 3-D joint body-wave and surface-wave tomography at 80 km depth from Obrebski *et al.* (2011). Green lines are the boundaries of the structural domains, pink line is the Cheyenne Belt, black dashed lines are the 80 km depth contour of the lithosphere–asthenosphere boundary from Miller & Levander (2009), perpendicular white dashed lines AA′ and BB′ correspond to the cross-sections shown in (c) and (d); 'C' refers to region C in Fig. 2. (c,d) NE–SW (AA′) and NW–SE (BB′) cross-sections, respectively, through the 3-D seismic tomography, modified from Obrebski *et al.* (2011); grey line locates the Moho; SN: Sierra Nevada range.

will not only significantly increase the melt production rates, but will thin the SCLM while recycling lithospheric material back into the convecting mantle (Anderson 2005; O'Reilly & Griffin 2010).

2.2 Lithospheric and upper-mantle structure

Geomorphological, geological, tectonic and seismological observations point towards an upwelling mantle plume as the source for the Yellowstone hotspot track (e.g. Pierce & Morgan 1992, 2009). However, the challenge since the end of the 90's is to better characterize and constrain the crustal and lithospheric structure beneath the Western USA. Several approaches have been implemented by gravimetry (e.g. DeNosaquo *et al.* 2009; Chaves & Ussami 2013), electrical conductivity (e.g. Kelbert *et al.* 2012), petrology and geochemistry (e.g. Griffin *et al.* 2004; Till *et al.* 2013). However, the most prolific method remains seismic tomography especially with the deployment of the EarthScope USArray in the early 2000's. Tomographic inversions allowed to constrain at various spatial scales the thermal, and/or rheological, and/or petrological structure of lithosphere and upper mantle below the Western USA (Chulick & Mooney 2002; Goes & van der Lee 2002; Fee & Dueker 2004; Yuan & Dueker 2005; Waite *et al.* 2005, 2006; Roth *et al.* 2008; Schutt & Dueker 2008; Schutt *et al.* 2008; Stachnik *et al.* 2008; Obrebski *et al.* 2010, 2011; Wagner *et al.* 2010, 2012; Yuan *et al.* 2010; Tian *et al.* 2011; Buehler & Shearer 2012; Levander & Miller 2012; Schmandt *et al.* 2012; Tian & Zhao 2012; Huang & Zhao 2013; Shen *et al.* 2013; Tauzin *et al.* 2013; Wagner & Long 2013;

Porritt *et al.* 2014; Hopper *et al.* 2014). Among all proposed tomographic models, which are consistent according to their resolutions (Becker 2012), we selected to illustrate our purpose the model from Obrebski *et al.* (2011) (Figs 1b–d) which is issued from the joint inversion of body-wave travel times and surface-wave phase velocities. Fig. 1(b) displays velocity anomalies at 80 km depth. The faster velocities located east of the YSRP correspond to the Wyoming cratonic lithosphere and are interpreted as cold, dense mantle. Griffin *et al.* (2004) further characterised this dense mantle as the SCLM. In this area, these authors further suggest a two-layer lithosphere with a well-developed lithological boundary at *ca*. 140 km depth. The upper layer consists of fertile depleted lherzolitic mantle rocks, while the lower layer is composed of a depleted metasomatized ultramafic lithology. We used the sections and data from Griffin *et al.* (2004) to calculate a subcontinental lithospheric mantle density profile below the Wyoming craton from 30 to 330 km depth (Appendix A1). As shown by both vertical cross-sections AA′ and BB′, the cratonic lithosphere can be locally up to 300 km thick (Figs 1c and d). More precisely, the eastern, northwestern and southeastern borders of the Wyoming cratonic lithosphere are delimited by 200–300 km high 'walls': these 'walls' make an angle of 20° and 45° with the vertical on the BB′ profile (Fig. 1d) and an angle of 40° to the NE on the AA′ profile (Fig. 1c).

The western part of the AA′ cross-section (Fig. 1c) displays from the surface down to 1000 km depth, three strips dipping west, which are red (described hereafter as 'hot') and blue (described hereafter as 'cold'). The top one wrapping the lithosphere is hot. Beneath the Yellowstone Caldera (YC), the bottom of this strip is located at 300 km depth, and reaches 600 km below the Sierra Nevada (SN), 1300 km away from the YC. At the vertical of YC, the underlying cold strip reaches a depth of 600 km. Dipping to the west, it reaches 1000 km depth at a distance of 900 km from YC. Finally, the last hot strip includes the deep section of what we consider as the Yellowstone plume. This strip also dips to the west penetrating into the lower mantle at a distance of around 1000 km from YC. Obrebski *et al.* (2010) suggested that the top hot strip represents material extracted from the Yellowstone plume during the last 16 Ma, which wormed its way between the cold subducted lithosphere fragments and eventually pounds at the lithosphere–asthenosphere boundary. James *et al.* (2011) and Liu & Stegman (2011) suggested that the intermediate cold strip represents subducted cold fragments of the Farallon plate up to 17 Ma old. The most intriguing observation provided by the tomographic models is that the hot mantle associated with the Yellowstone plume is thousand kilometres wide at 1000 km depth, but only a few 100 km wide in the upper mantle (Smith *et al.* 2009) (Fig. 1d). This observation is consistent with the superswell concept developed by Davaille (1999): hotspot plumes grow from the top of a rising hot dome. Such structures are well known from large-scale numerical models with a large viscosity contrast between upper and lower mantle (Zhang & Yuen 1995; Zhang & Yuen 1996; Cserepes & Yuen 2000), which leads to a drastic reduction of the superswell size when crosses the 660-km interface (Cserepes & Yuen 2000; Smith *et al.* 2009). However, the presence of an extremely large horizon of cold material surrounding the plume at 600 km depth (fig. 10e in Obrebski *et al.* 2011) more likely suggests a cold boundary layer separating the upper and lower mantle beneath the western coast of USA. Cold fragments of Farallon plate are included in this horizon (Obrebski *et al.* 2011; Fig. 2). According to Liu & Stegman's (2011) model, the buoyancy of these fragments results from the loss of mechanical continuity of the subducting Farallon plate consequently to its tearing 17 Ma ago. Fukao & Obayashi (2013) showed that most of the subducted plates around the Pacific stagnate above the 660-km interface while others float above 1000 km depth. Only few subducting plates plunge directly into the lower mantle. This suggests that crustal material and depleted mantle may separate at depth during subduction, endorsing so a petrological layering above or below the spinel-perovskite transition zone (Karato 1997; Mambole & Fleitout 2002; Lee & Chen 2007). Furthermore, the presence of a superswell may prevent the penetration of cold lithospheric fragments into the lower mantle. These facts have two major consequences for the mantle below the continental side of the subduction zone: (i) convection in the upper mantle separates from the one within the lower mantle (Richter & Johnson 1974); (ii) the mantle above the 660 km or 1000 km interface is considerably cooled by the lithospheric fragments of the subducted Farallon plate floating at 600–700 km depth (Rabinowicz *et al.* 1980). Consequently, the imaged fast seismic velocity regions in between 400 and 700 km depths (Fig. 1c) represent the trapped remnant slab lying on the 660 km depth discontinuity, and eventually also the overriding cooled mantle above (e.g. James *et al.* 2011). Finally, subducting fragments of the Farallon plate plunging into the lower mantle are restricted to an area located further east, for example, outside of the Yellowstone superswell (Liu *et al.* 2008; Liu & Stegman 2011; Sigloch 2011; Pavlis *et al.* 2012; Sigloch & Mihalynuk 2013).

The BB′ cross-section (Fig. 1d) shows that the low velocity zone beneath the YC connects the Moho to the deep hot horizon at ∼1000 km depth. The axis of the Yellowstone plume tail is then necessarily defined within this low velocity column. Consequently, its vertical undulations below YC footprint the displacement of the plume induced by the toroidal flow resulting from the difference in rotation poles and angular velocities between the North American plate and the 660 km deep mantle flow of the subducting Juan de Fuca slab (Zandt & Humphreys 2008).

The 410- and 660-km discontinuities were investigated, for example, with *P*- and *S*-wave receiver functions and with *P*-to-*S* converted phases (Sheehan *et al.* 2000; Tauzin *et al.* 2013). Fig. 2(a) displays the topography of both discontinuities roughly parallel to the BB′ profile (Sheehan *et al.* 2000). At the mantle plume axis, the 410-km discontinuity has a downward topography of 20 km corresponding to at most an excess temperature of 180 °C (Yuan & Dueker 2005; Smith *et al.* 2009). In contrast, the 660-km discontinuity has a wavy 40–50 km peak-to-peak topography which most plausibly represents mantle containing ponded melt (Sheehan *et al.* 2000; Schmandt *et al.* 2012). More precisely, this topography is actually formed by the combination of two curves. First, there is a 'ridge' centred within the plume axis with a height of 20 km and a width of 150 km. Then, there is a stair-like curve 200-km wide on each side of the plume axis. The 410- and 660-km discontinuities are consistent among themselves, while somewhat staggered (i.e. the 'ridge' on the 410-km discontinuity is offset to the NW), which we attribute to toroidal subcontinental mantle flows.

The regional topography of the 410-km discontinuity mapped by Eagar *et al.* (2010) (Fig. 2b) exhibits ups and downs with maximum magnitude at 30 km corresponding to descending and ascending mantle flows, respectively. It is noteworthy that the most recent volcanic activities outside the YC (four yellow stars in region C in Fig. 2b; Shervais & Vetter 2009) are located above a topographic minimum of the 410-km discontinuity. They may lie above an ascending mantle flow. This region also overlaps with a local minimum of the seismic velocities of the 80 km deep horizon of Obrebski *et al.*'s (2011) tomographic model (Fig. 1b). Below region C, there is a quasi-continuous and quasi-vertical low seismic velocity anomaly extending from 80 km depth down to 800 km depth into the few

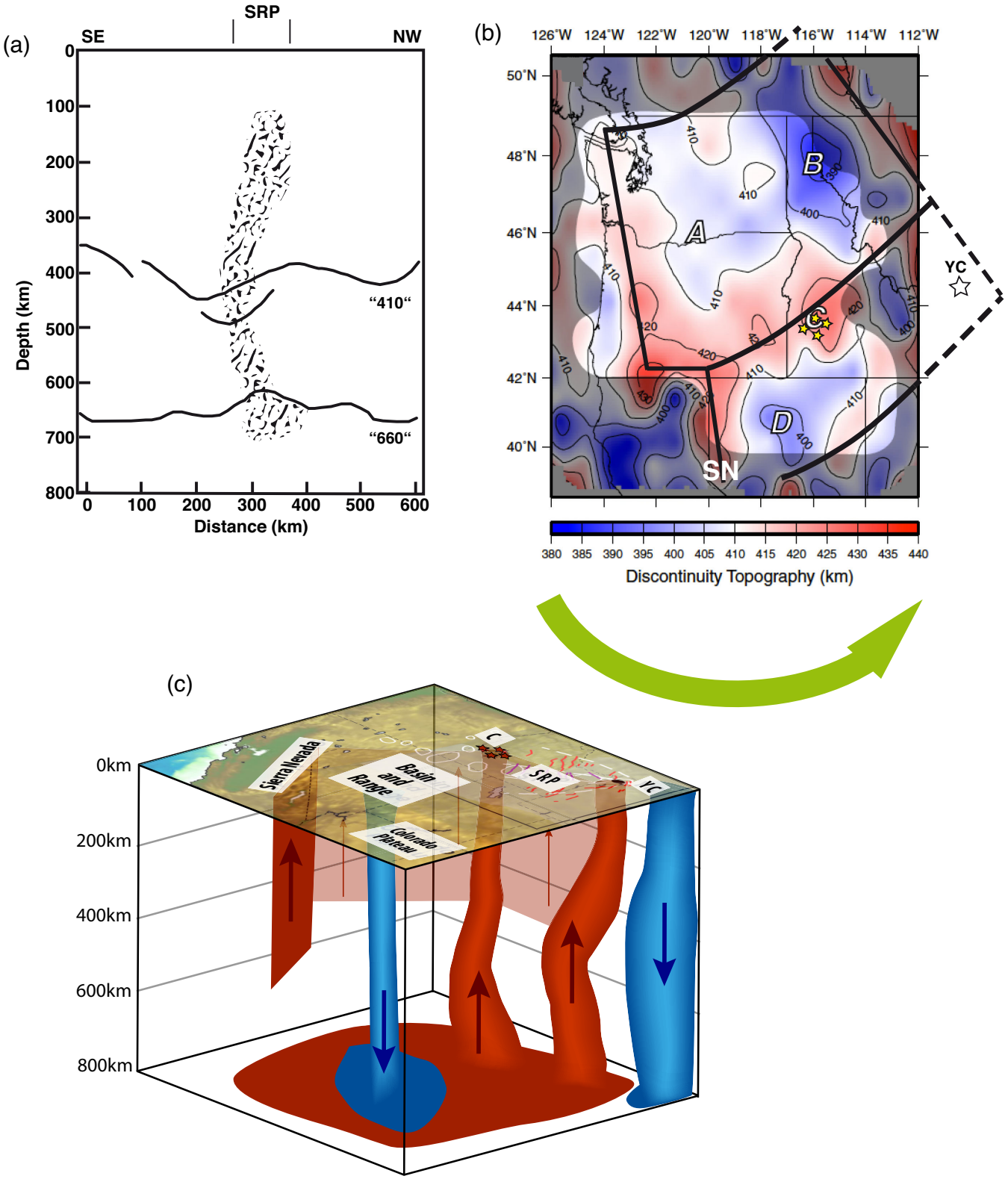

Figure 2. 410- and 660-km discontinuities. (a) Topography of the 410- and 660-km discontinuities and the ascending plume (hachured zone) along an SE–NW cross-section modified from Sheehan *et al.* (2000). (b) Interpretation of polygonal convective cells on the map of the 410-km discontinuity topography from Eagar *et al.* (2010). The cells are distorted by a rotation due to the toroidal flow of mantle induced by the Juan de Fuca slab subduction (green arrow; Zandt & Humphreys 2008); white star locates the YC, yellow stars locate the most recent volcanic activity (−1.8 to −0.8 Ma) of high-K alkali basalts and low-K tholeiitic basalts from Shervais & Vetter (2009); SN: Sierra Nevada. (c) 3-D sketch of the ascending and descending flows below the Sierra Nevada–Basin and Range–Yellowstone–Snake River Plain region.

thousand kilometres wide hot anomaly of the Yellowstone plume (Obrebski *et al.* 2011). This suggests that the volcanoes of region C are linked to a mantle plume, which roots at the same 800 km deep hot anomaly as the Yellowstone plume. Moreover, region C forms an integral part of an SW–NE striking 'hot valley' of the regional 410-km discontinuity (i.e. downward deflection of the 410-km discontinuity, red regions in Fig. 2b). To the west, this line crosscuts the ∼NS hot line of the SN, while to the east it contours the axis of the Yellowstone plume. Then, the linear 410-km hot anomaly tracks back southwest, south of the YSRP. Finally, the hot line is interrupted at 40°N–115°W inside the Basin and Range and above a 'very hot spot' on the 300 km deep tomographic horizon. Note that the southern segment of the 410-km hot line is well seated above a very extended 600 km deep cold horizon, which represents the 660-km deep cold flow driven by the subducted Farallon plate (Obrebski *et al.* 2011). From this analysis, it results that a hot mantle flow contours the YSRP on three sides. The northern branch of this hot flow, and the one contouring the eastern part of the Yellowstone plume, originate from the ∼1000 km wide and 800-km deep hot domain centred below the Yellowstone plume. In contrast, the southern branch is restricted to the upper mantle. Finally, the 'rectangle' of vertical flows can be closed by considering the ascending flow, from south to north, within the SN and the California ranges (Fig. 2). The cold region located just east of the SN and the California hot line follows the eastern California Shear Zone. It is simultaneously very cold on the 410-km deep topographic map and on the 300 km and 600 km deep tomographic horizons (Fig. 1). This indicates that the return cold flow of the four ascending hot vertical sheets is essentially confined within this cold area. These four ascending hot sheets form a box enveloping the Yellowstone plume, which is clearly more elongated in the east–west direction (∼1000 km) than in the north–south one (300 km). These 300-km deep east–west elongated structures may be biased in the tomographic images by the prevalence of the earthquakes in the western Pacific. However, Gilbert *et al.* (2003) made the same observation and underlined its geodynamical importance concluding that 'the thermal variations of the 410 km depth are influenced by small scale convective flow in the upper mantle, while the convection in both upper and lower mantle influences the depth of the 660-km discontinuity'. More precisely, we establish that 200–300-km large roll-type convective waves with axis parallel to the plume track develop on the western side of YC, while the convective flow in the planes parallel to the plume track have a horizontal size of ∼1000 km. Fig. 2(c) summarizes the above description in a 3-D cartoon.

A detailed tomographic model of the crust and upper mantle from Yuan *et al.* (2010) is shown in Fig. 3. It represents a 600 km long and 150 km deep SW–NE cross-section centred on the YC. As previously described in Fig. 1(c), the fast shear velocities characterizing the Wyoming cratonic lithosphere are located to the east of the ascending plume. Surprisingly, a 100-km long fast velocity zone is observed just above the plume axis. This zone is delimited at about 70 km depth by an interface identified by a downward negative wave velocity gradient of Common Conversion Points (CCP). Other CCP interfaces with paired of negative and positive gradients are detected to the west, at the boundary between the mantle plume and the Wyoming craton. Hopper *et al.* (2014) confirm these observations, which strongly suggest the presence of melt east to the plume axis between 50 and 80 km depth. It is also important to note that there is a northeastward lateral offset of 70–100 km between the plume axis and the location of the YC (Fig. 3).

The crustal thickness map of Western USA (Shen *et al.* 2013) evidences a strong dissimilarity from west to east (Figs 1, 3 and 4). At the Pacific coast, the crust is 25 km thick and then thickens rapidly to 30–35 km reaching 50–55 km at the Wyoming craton, with lateral variations at ±5 km (Figs 4b and c). If a thickness of 30–35 km is 'normal' for continental crust, the eastern cratonic crust is abnormally thick with a thickness at 45–50 km just below the YSRP. Furthermore, the gravimetric data highlight a strong negative Bouguer anomaly down to −200 mGal over the Western USA except along the coast where the crust is the thinnest (Figs 4a and d). We calculated the isostatic anomaly by retrieving to the Bouguer anomaly the difference between the compensated crustal thickness and the observed crustal thickness of Shen *et al.* (2013) (Fig. 4e). The isostatic anomaly is positive west of the YC and the Snake River Plain, and becomes negative in the YC area, which clearly indicates a lack of mass, that is, the presence of buoyant material such as melt below the YC.

2.3 Crustal and lithospheric deformation

The YSRP region is characterized by an intense seismic activity (Fig. 5), considered as the most important of the Intermountain Seismic Belt extending from northern Montana to northern Arizona. Instrumental seismic catalogues contain up to 900–1000 events per

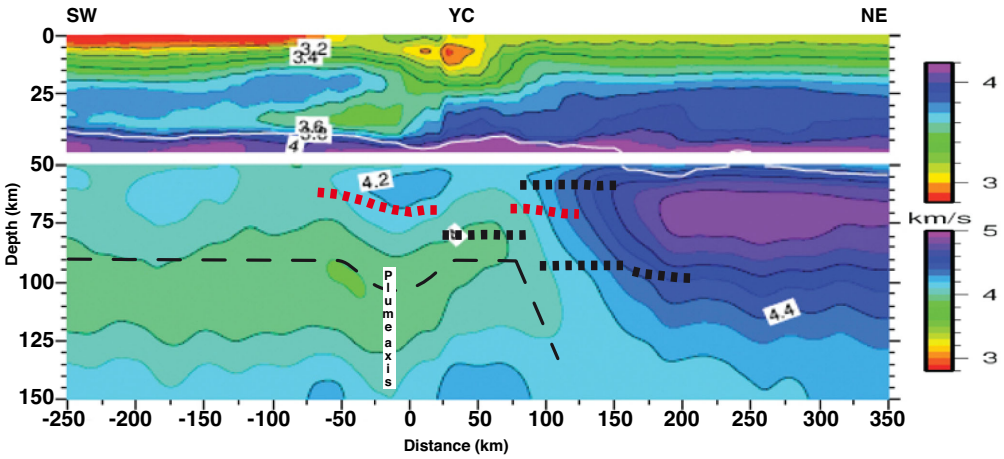

Figure 3. Shear velocity tomography and Common Conversion Point (CCP) polarities in thick dashed lines (red: negative, black: positive), modified from Yuan *et al.* (2010); gray line locates the Moho; the ascending plume and the 1340 °C limit from our plume model (see Section 4 for details) are positioned.

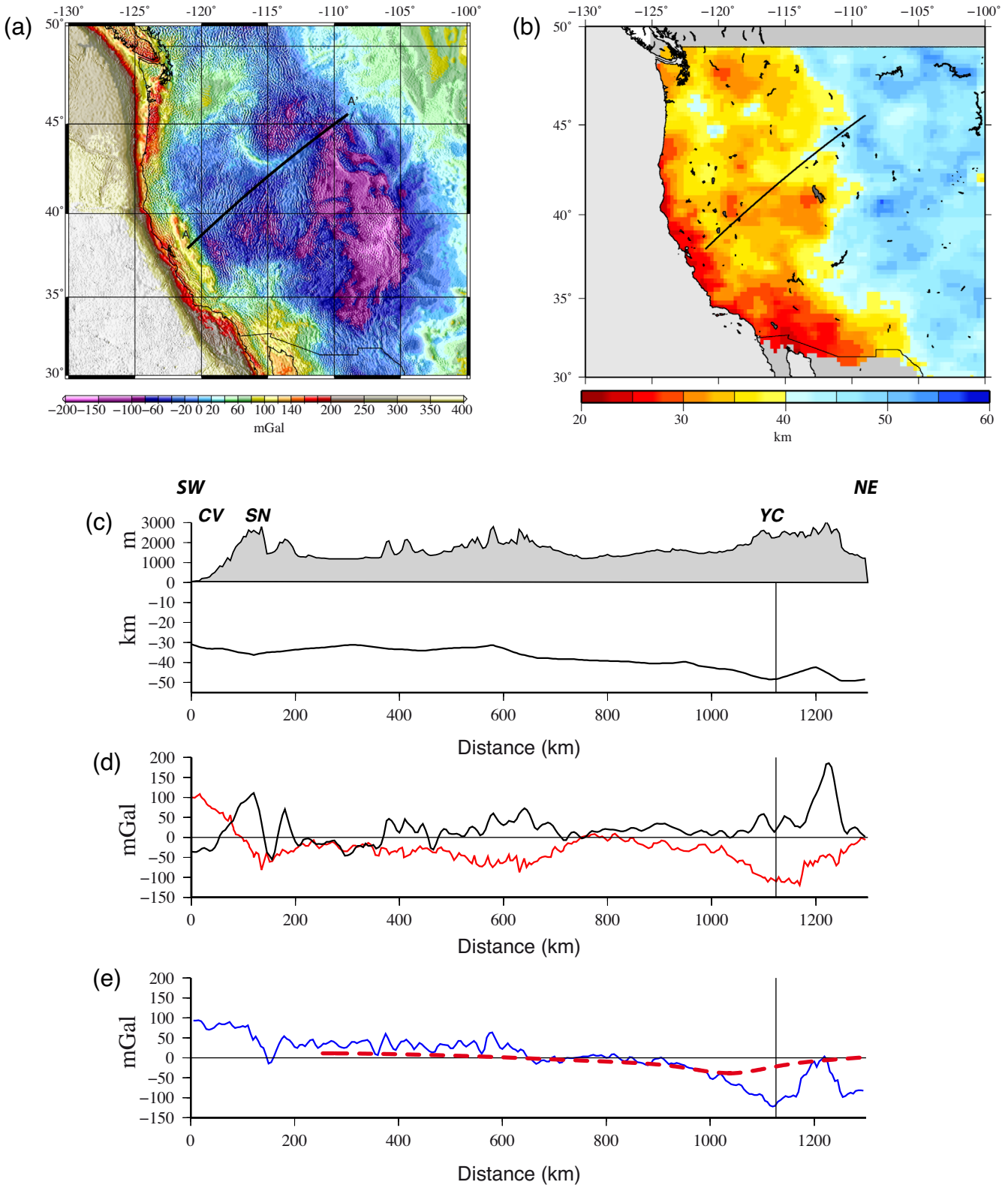

Figure 4. Gravity observations. (a) Map of the Bouguer anomaly over the Western USA extracted from the World Gravity Map (Bonvalot *et al.* 2012). Profile AA′ of Fig. 1 is indicated. (b) Map of the crustal thickness over the Western USA (Shen *et al.* 2013). (c) SW–NE cross-section of topography and crustal thickness (profile AA′). (d) Gravity (black line, GRACE Gravity Model CGM02) and Bouguer anomaly (red line) along the profile AA′. (e) Isostasic anomaly (blue line, Bouguer anomaly minus the difference between a compensated crustal thickness and the observed crustal thickness) and the gravity associated with our plume model (dashed red line). This last one is symetric as our model and shifted by 100 km to the SW at the vertical to the lithospheric plume axis (Fig. 5b).

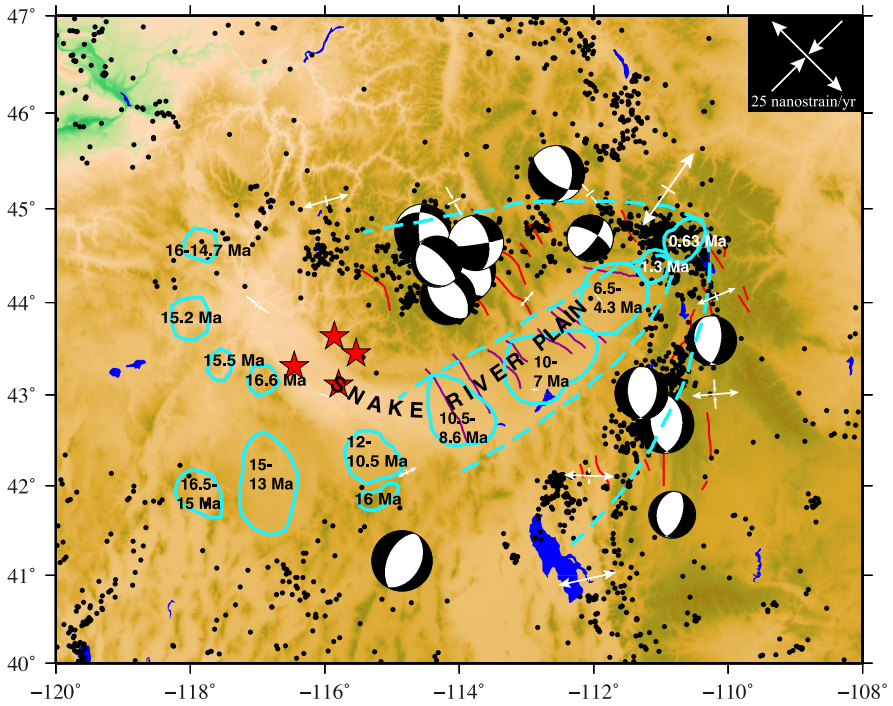

Figure 5. Map of the seismicity from 1973 to present (NEIC database) with the focal mechanisms for events of $M_w \geq 4.6$ from 1983 to present (CMT catalogue from USGS). The strain-rate tensors are derived from GPS measurements modified from McCaffrey *et al.* (2013). In light blue, the tectonic parabola of present-day deformation and the successive calderas with their ages along the hotspot track of Yellowstone plume modified from DeNosaquo *et al.* (2009); red stars, violet and red lines are as in Fig. 1.

year (Farrell *et al.* 2009) with observed maximum magnitudes M_s at 7.0–7.5. The most recent major events are the 1959 M_s 7.5 Hebgen Lake, Montana, the 1975 M_s 6.1 Norris Junction earthquake, and the 1983 M_s 7.3 Borah Peak earthquakes, Idaho (Husen & Smith 2004; Farrell *et al.* 2009; Smith *et al.* 2009). The Hebgen Lake and Norris Junction earthquakes occurred 25 km north to and within the 0.63 Ma old YC, respectively. North to the YSRP, the seismicity is elongated along the E–W direction whereas on the southern side, in the Teton region, it has an NE–SW trend sub-parallel to the Eastern Snake River Plain (ESRP) direction. At YC, seismicity is less frequent and occurred as swarms with events characterised by magnitude not greater than $M_w = 4.0$–4.2, and generally with a ∼N–S trending (Waite & Smith 2002; Shelly *et al.* 2013). The seismicity concentrates over the cold and thick cratonic lithosphere surrounding the Yellowstone hotspot track, and within the most recent caldera. In contrast, seismicity is absent in the whole Snake River Plain and along the 17 Ma old SW–NE hotspot track (Fig. 5). The described seismicity draws the well-known tectonic parabola (Pierce & Morgan 1992; DeNosaquo *et al.* 2009; Smith *et al.* 2009). This parabola involves active NW–SE trending faults (red lines in Fig. 5) in the northern part and N–S trending in the eastern and southern parts. In contrast, its internal part corresponding to the ESRP contains dykes (purple lines in Fig. 5) with a NW–SE trend (Kuntz *et al.* 1992; Pierce & Morgan 1992; Parsons *et al.* 1998). Focal mechanisms of major seismic events as shown in Fig. 5, point towards principally NE–SW extension to the north of the ESRP, and E–W extension within the area between the 0.63 Ma YC and the southwest of the parabola. The mean velocity of this extension has been measured by GPS at 2–4 mm yr^{-1} (Pickering White *et al.* 2009; Smith *et al.* 2009).

Permanent GPS surveys and recurrent measuring campaigns at several hundred sites since the early nineties reveal horizontal stretching consistent with the seismicity (white arrows in Fig. 5). Strain-rate tensors determined from GPS measurements confirm the NE–SW extension to the north of ESRP and E–W extension to the south, of about 5 nstrain yr^{-1} (i.e. $\sim 1.5 \times 10^{-16}$ s^{-1}) up to 25 nstrain yr^{-1} (i.e. $\sim 8 \times 10^{-16}$ s^{-1}) at the northeast termination of the parabola, whereas no deformation is detected in the ESRP (Smith *et al.* 2009; Payne *et al.* 2012; McCaffrey *et al.* 2013). Moreover, GPS observations combined with levelling and InSAR observations reveal alternative uplift and subsidence up to 2 cm yr^{-1}, commonly interpreted as recharge and discharge episodes of the crustal magma reservoirs and are furthermore directly linked to the presence of a mantle plume (Saunders *et al.* 2007; Pickering White *et al.* 2009; Pierce & Morgan 2009). Similarly, earthquake swarms are considered triggered by fluid activity in dykes correlating seismic activity and periods of uplift and subsidence (Waite & Smith 2002; Farrell *et al.* 2009; Smith *et al.* 2009; Shelly *et al.* 2013).

The pattern of regional deformation displays nearly no seismicity nor horizontal deformation in the interior of the ESRP where volcanic centres are older than 4.3 Ma. Nevertheless, volcanism indicates a long-term extension in the ESRP, estimated at about 6.8 m per 1000 yr and accommodated by magma intrusions within the dyke network in the ESRP (Parsons *et al.* 1998). There, 1-m-by-5 km dykes, randomly distributed across the plain, yield to a local minimum extension rate of 1.1×10^{-16} s^{-1}, a value comparable to the GPS strain-rate measurements at $\sim 1.5 \times 10^{-16}$ s^{-1}.

2.4 Lithospheric viscosity estimation

Because of temperature and chemical composition variations, the mantle underneath the YSRP, from depths of 30–100 km in the lithosphere and from depths of 100 to ∼200 km in the asthenosphere, has a density contrast $\delta\rho$ with the surrounding cratonic lithosphere that likely represents a few percents (i.e. a few times

34 kg m^{-3}) (Poudjom Djomani *et al.* 2001; Appendix A1). It results that the lithosphere–asthenosphere boundary pushes the surrounding cratonic lithosphere laterally, in a similar manner to the way the asthenosphere pushes the base of oceanic lithosphere at spreading centres (Turcotte & Schubert 2002). The difference of stress integrated over a cratonic lithosphere of height $H = \sim$200 km represents a force F equal to

$$F = \delta\rho\, gH^2/2, \tag{1}$$

where g represents the gravity constant. Assuming that $\delta\rho = 34$ kg m^{-3} (i.e. a minimum value for the density contrast), this force reaches $\sim 6.6 \times 10^{12}$ N m^{-1}, corresponding to a mean extensional stress σ equal to 66 MPa through the 100-km thick crust and upper mantle of the YSRP, or equal to 33 MPa through the 200-km thick surrounding cratonic lithosphere. Both values exceed the 10 MPa maximum stress drop of normal-fault earthquakes (Kanamori & Anderson 1975; Jackson & Blenkinsop 1993). Regenauer-Lieb *et al.* (2008) estimated that a tensile stress of 384 MPa is required to steadily stretch a lithosphere, if it is free of interstitial melt or fluids. Because (i) the concentration of melt and fluids partly explains the low seismic velocities of the lithosphere below the YSRP and (ii) the rheology of the Wyoming cratonic lithosphere was weakened by melt intrusions during the Proterozoic (Chamberlain *et al.* 2003), we must expect that the critical tensile stress for plastic deformation is much closer to 10 MPa than to 384 MPa. It is inferred that, around the YSRP, the minimal tensile stress σ_{ten} and extensional strain-rate γ are 10 MPa and $\sim 10^{-16}$ s^{-1}, respectively. Thus, the minimum effective viscosity of the lithospheres is

$$\mu_{\text{eff}} = \sigma_{\text{ten}}/2\gamma = 5 \times 10^{22} \text{ Pa s}. \tag{2}$$

Clearly, this estimation represents a minimum value and could be easily two orders of magnitude greater given common extrapolations from experimentally evaluated power-law creep parameters (e.g. Bürgmann & Dresen 2008). For instance, an effective viscosity of $\sim 10^{24}$ Pa s is estimated for oceanic plates at subduction zones (DeBremaecker 1977), which contains much less fluids or melt than around the YSRP.

Concerning the asthenosphere underneath, the global inversion of glacial isostatic data in cratonic areas displays a minimum viscosity of $\sim 10^{20}$ Pa s grading up to $\sim 10^{21}$ Pa s at its base, that is, at $\sim$410 km depth (Mitrovica & Forte 2004), and which remains roughly constant down to 670 km depth (Spada *et al.* 1992). However, below the northwestern part of the USA, the low viscosity layer is much more complex. The spectrum of published estimated mantle viscosities ranges from 5×10^{17} to 5×10^{19} Pa s and they are applied to a thick section of the upper mantle (Bills *et al.* 1994, 2007; James *et al.* 2000; Pollitz 2003). This may result from both partial melting and high volatiles content of the asthenosphere, which, as stated above, is particularly important below the western part of the USA.

3 DESTABILIZATION MODEL OF THE WYOMING LITHOSPHERE TO THE EAST OF THE YELLOWSTONE PLUME

The vertical impingement of the Yellowstone plume into the 200–300 km thick cratonic lithosphere indicates that the lower half of the craton is delaminated at the same velocity that the axis of the plume migrates with respect to the American continent. On Earth, there is no other example of a so fast delaminated lithosphere. From their modelling of hydrodynamical instability leading to the delamination of the lithosphere, Houseman & Molnar (1997) concluded that between 50 per cent (for rheological parameters representative of dry olivine) and 70 per cent (for wet olivine) of the continental lithosphere could be delaminated. However, this process is slow as it requires at least 10–15 Ma to develop (Bird 1979; Houseman & Molnar 1997; Morency & Doin 2004). During such a time period, the Yellowstone plume would be squeezed under the lithosphere at 200 km depth over a distance of 250 km, which is not observed. Actually, most authors consider delamination cases when (i) the density anomalies driving the instability result from temperature anomalies generated during collision or extensional tectonic processes and (ii) the lithosphere and asthenosphere have usual temperature and stress dependent rheologies. Because of the Proterozoic subduction of oceanic lithosphere below the Wyoming craton, we consider that the density anomalies driving the delamination have a chemical origin, and thus are irreversible. This is different from density heterogeneities resulting from mantle convection below continents, which are due to reversible thermal anomalies. Here, the delamination following the Proterozoic underthrusting essentially results from the development of a diapiric instability, which is irreversibly unstable, whereas the thermal instability due to tectonics is only marginally unstable. According to the principle of exchange of stability, both the growth rate and the characteristic wavelength of the diapiric instability can be derived from a linear stability analysis of diapiric instability due to the Proterozoic underthrusting (Conrad & Molnar 1997; Neil & Houseman 1999). Another very important assumption of our modelling is that Proterozoic magmatic intrusions irreversibly weakened the whole Wyoming crust and lithosphere. This means that they do not necessarily behave as non-Newtonian power-law fluids whose stress $\tau_{i,j}$ and strain-rate tensors $\dot{\varepsilon}_{i,j}$ are related by

$$\tau_{i,j} = C\, \dot{\varepsilon}_{i,j} \dot{\varepsilon}^{\frac{1-n}{n}}, \tag{3}$$

where $\dot{\varepsilon} = (\dot{\varepsilon}_{k,l}\dot{\varepsilon}_{k,l})^{\frac{1}{2}}$ is the second invariant of the strain-rate tensor, C is a proportionality factor depending on temperature and n is a power-law constant close to $\sim$3. Deformation of continental crust and lithosphere is actually more likely controlled by movements of blocks along pre-existing faults of various orientations (Ismail-Zadeh *et al.* 2002), that is, no deformation occurs below stresses of the order of 10 MPa, whereas deformation is likely to be plastic above this limit. Furthermore, we assume that dynamic friction along such pre-existing faults does not depend upon the strain rate: such behaviour is then best described by a perfectly plastic material, which does not exhibit work-hardening, but flows plastically under constant stress. In that case, the stress–strain relationship obeys the Von Mises equations (Prager & Hodge 1951):

$$\tau_{i,j} = \frac{\kappa}{\dot{\varepsilon}_{i,j}}, \tag{4}$$

where κ is the yield limit. The second invariant of the stress tensor, $\tau = \tau_{k,l}\tau_{k,l}$, equals the yield limit, κ, for any non-zero strain rate. When $\tau < \kappa$, there is no plastic deformation and hence no motion along faults. A comparison of eqs (3) and (4) shows that the perfectly plastic rheology can be considered as a limit to the non-Newtonian power-law rheology as n tends to infinity. In the following, we shall refer to a purely plastic material by this limit with $C = \kappa$. Then, assuming that the lithosphere has either a power-law or a purely plastic rheology, we explore the conjunction of the four possible following factors: (i) the lower part of the Wyoming lithosphere is negatively buoyant (Griffin *et al.* 2004); (ii) the density contrast between the mantle beneath the YC and the surrounding cratonic lithosphere induces a tensile stress $\sigma_{\text{ten}} \geq 10$ MPa; (iii) the $\sim$100 km deep magmatic sills on the eastern side

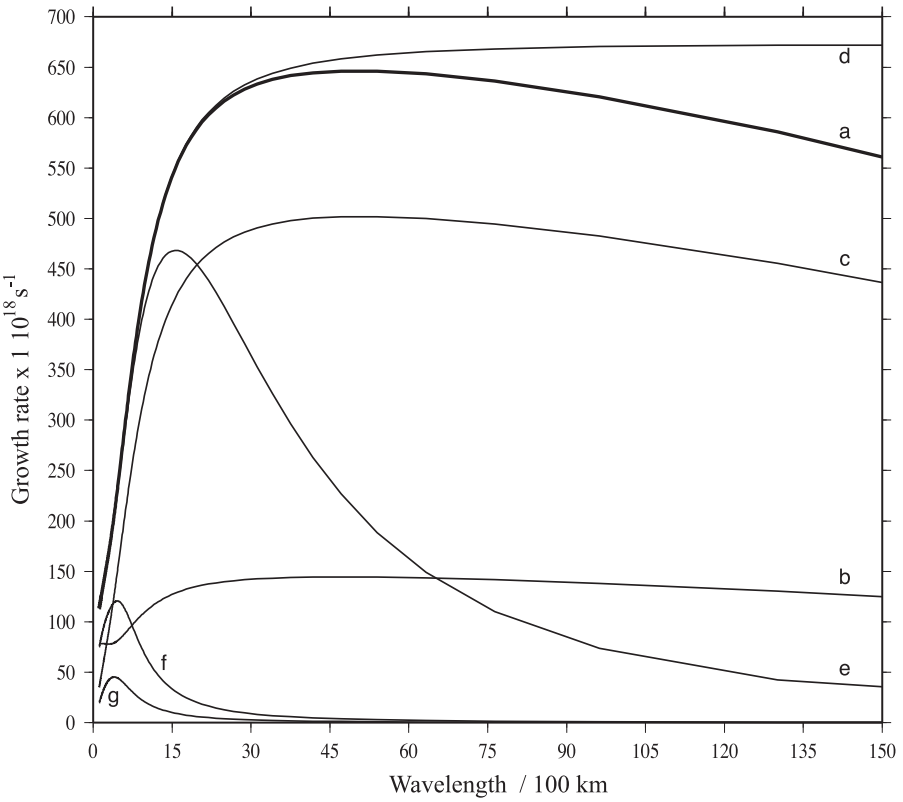

Figure 6. Instability analysis for $n = 3$, that is, the lithosphere deforming by plastic creep. (a) reference curve where $\eta_1 = 5 \times 10^{22}$ Pa s, $\eta_2 = 10^{18}$ Pa s, $\gamma = 10^{-16}$ s^{-1}, $\Delta\rho = 1$ per cent; (b) idem as (a) but $\Delta\rho = 0$ per cent; (c) idem as (a) but $\gamma = 0$; (d) idem as (a) but $\eta_2 = 10^{16}$ Pa s; (e) idem as (a) but $\eta_2 = 10^{20}$ Pa s; (f) idem as (a) but $\eta_2 = 10^{22}$ Pa s; (g) idem as (a) but $\eta_2 = 5 \times 10^{22}$ Pa s.

of the Yellowstone plume (displayed in the tomographic model of Yuan *et al.* 2010), mechanically decouple the negatively buoyant lower part of the lithosphere from its upper part; (iv) the partially molten and fluid rich asthenosphere below the western side of the USA has a linear viscosity and is particularly thick (Kelemen *et al.* 1997).

We use Ismail-Zadeh *et al.*'s (2002) formalism to quantify the growth of diapiric and stretching instabilities, detailed derivations being given in Appendix A2. In the following, we assume that the negatively buoyant section of the lithosphere (thereafter named Layer 1) has a constant thickness $h_1 = 100$ km. The lithosphere deforms either by plastic creep (i.e. $n = 3$), or behaves as a perfectly plastic material (i.e. $n = \infty$) and flows under a constant stress C of several 10 MPa, at a constant rate $\gamma \sim 10^{-16}$ s^{-1}. We deduce that the effective viscosity of the lithosphere $\eta_1 = \sigma/2\gamma$ may range between $\sim 5 \times 10^{22}$ Pa s and $\sim 2.5 \times 10^{24}$ Pa s. Finally, we assume that, prior to the erosion of the Wyoming lithosphere by the Yellowstone plume, the underlying asthenospheric horizon (thereafter named Layer 2) has: (i) a constant thickness $h_2 = 100$ km and (ii) a viscosity η_2 ranging between 10^{18} Pa s and 10^{20} Pa s (e.g. Rabinowicz *et al.* 2012). The contrast of density $\Delta\rho$ between the overlying dense part of the Wyoming lithosphere (Layer 1) and the Yellowstone plume mantle (Layer 2) is taken equal to 34 kg m^{-3} ($\sim$1 per cent of the mantle density, i.e. a value chosen in the lower range of possible estimates). Appendix A2 details how we computed the growth rate of the instabilities. Figs 6 and 7 display these growth rates versus the wavelength assuming that the dense section of the Wyoming lithosphere is decoupled from the overlying buoyant one as stated above (free-slip top boundary condition). Cases displayed in Fig. 6 assume a power-law rheology with $n = 3$ (eq. A13b in Appendix A2), while those of Fig. 7 assume a perfectly plastic (i.e. $n = \infty$, eq. A15 in Appendix A2).

In Fig. 6, profile (a) represents the growth rate when $\eta_1 = 5 \times 10^{22}$ Pa s, $\eta_2 = 10^{18}$ Pa s, $\Delta\rho = 1$ per cent and $\gamma = 10^{-16}$ s^{-1}. The most instable perturbation has a wavelength at $\sim$4500 km and a growth rate $p = \sim 6.5 \times 10^{-16}$ s^{-1} = 1/50 Ma. When we assume instead that $\Delta\rho = 0$ per cent, that is, that the lithosphere is simply stretched (profile b), or that $\gamma = 0$, that is, that the contribution of the stretching instability (e.g. boudinage) is negligible with respect to the gravitational instability (profile c), then we obtain maximum growth rates of $\sim 1.5 \times 10^{-16}$ s^{-1} and $\sim 5 \times 10^{-16}$ s^{-1}, respectively. These values prove that the diapiric instability has a similar importance on lithospheric delamination as a stretching instability. When $\eta_2 = 10^{16}$ Pa s, the critical wavelength becomes infinite (profile d). When $\eta_2 = 10^{20}$ Pa s, the critical wavelength reaches $\sim$1500 km and the maximum growth rate $p = \sim 4.5 \times 10^{-16}$ s^{-1} = $\sim$1/65 Ma (profile e). Finally, when the viscosity contrast between Layer 1 and Layer 2 is small, with a factor 5 (profile f) or even 1 (profile g), the critical wavelength reaches more reasonable values (400–600 km), but the maximum growth rate of the instability becomes extremely weak ($\sim$1/500 Ma). These results are reminiscent to those obtained by Richter & Daly (1978), who showed that the large horizontal scales of mantle convection result from a large lithosphere/asthenosphere viscosity contrast. Actually, even in the most favourable case represented here by profile (a), we see that instabilities from negative buoyancy and tensile stresses result in complete large-scale delamination of the Proterozoic dense layer in a few hundred Ma. This would induce the formation of a subduction zone. As this is not observed, a purely viscous rheology is not adequate to describe geodynamical process in this region. As a

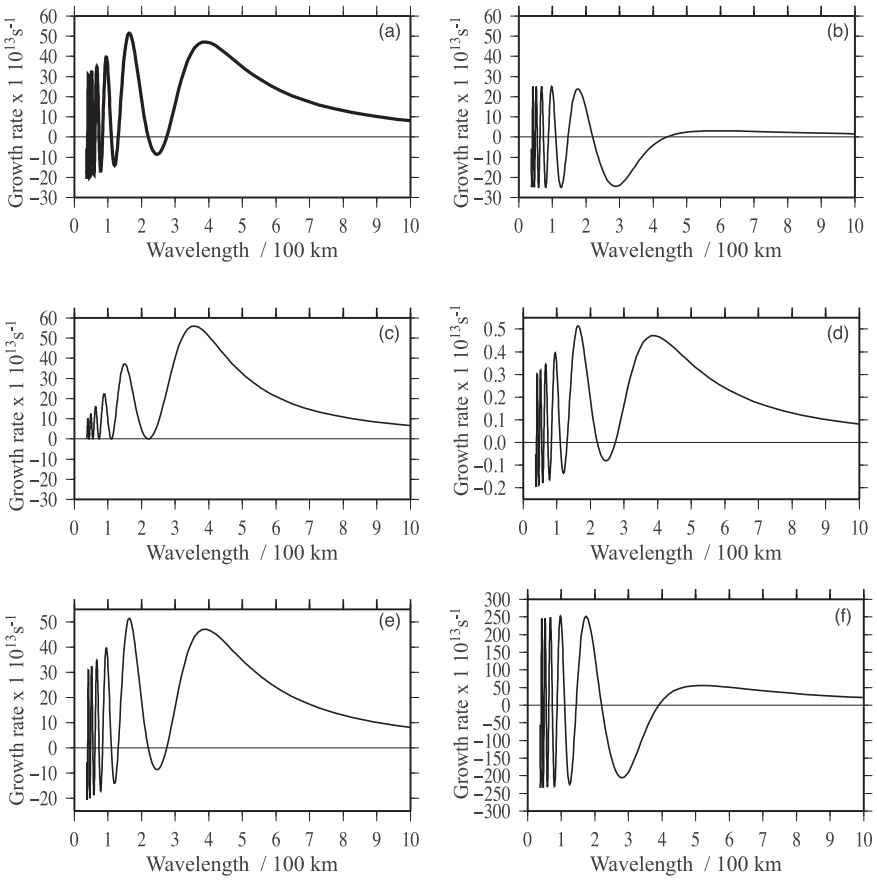

Figure 7. Instability analysis for $n = \infty$, that is, the lithosphere is perfectly plastic. (a) Reference curve where $\eta_1 = 5 \times 10^{22}$ Pa s, $\eta_2 = 10^{18}$ Pa s, $\gamma = 10^{-16}$ s^{-1}, $\Delta\rho = 1$ per cent; (b) idem as (a) but $\Delta\rho = 0$ per cent; (c) idem as (a) but $\gamma = 0$; (d) idem as (a) but $\eta_2 = 10^{20}$ Pa s; (e) idem as (a) but $\eta_1 = 5 \times 10^{24}$ Pa s and $\gamma = 10^{-18}$ s^{-1}; (f) $\eta_1 = 8 \times 10^{23}$ Pa s, $\eta_2 = 10^{18}$ Pa s, $\gamma = 6 \times 10^{-17}$ s^{-1}, $\Delta\rho = 1$ per cent.

consequence, the only admissible assumption is that the Wyoming lithosphere is not deformable below a specific stress threshold, and obeys to a plastic rheology above this threshold.

Cases presented in Fig. 7 show that the situation dramatically changes when the rheology of the lithosphere is assumed perfectly plastic (i.e. $n = \infty$). For instance, profile (a) obtained using the same parameter values as for profile (a) of Fig. 6, shows that the critical wavelength of the instability is ~170 km and that the growth rate reaches 5×10^{-12} s^{-1} = 1/6000 yr. Growth-rate variations when $\Delta\rho = 0$ per cent (profile b) and $\gamma = 0$ (profile c), respectively have similar amplitudes (i.e. a maximum growth rate of 2×10^{-12} s^{-1} and of 5×10^{-12} s^{-1}, respectively), indicating once more that diapiric and stretching instabilities play an equivalent important role on lithospheric delamination. But the shape of both curves differs. When $\Delta\rho = 0$ per cent (profile b), the growth rate reaches its maximum for a wavelength of ~170 km after behaving quasi-sinusoidal. The curve presents positive and negative peaks, implying that when the growth rate is positive, the instability grows with time, while it is damped in the opposite case. When $\gamma = 0$ (profile c), the growth rate has a damped sinusoidal shape with a minima just above zero, and reaches a maximum for a wavelength of ~400 km, that is, twice the thickness of Layer1 + Layer2. Profile (d) displays the growth rate when η_2 is increased from 10^{18} Pa s to 10^{20} Pa s. Actually, curve (d) is quasi-identical to curve (a), provided that the scale of the growth rate axis is divided by 100. This indicates that the amplitude of the growth-rate curve depends linearly on η_1/η_2. Finally, we consider the case where $\eta_1 = 5 \times 10^{24}$ Pa s, $\gamma = 10^{-18}$ s^{-1} and thus that $\sigma = 2\eta_1\gamma = 10$ MPa (profile e on Fig. 7). Curves (e) and (a) are virtually the same. This shows that the exact magnitude of lithospheric effective viscosity does not play an important role in its destabilization, but instead, it is the stress level beyond which the lithosphere deforms that is of great importance.

We have also computed the growth-rate curve when $n = \infty$ by setting a no slip condition at the top of Layer 1. That boundary condition supposes that the deepest and densest section of the lithosphere is pegged (mechanically coupled) to its overriding buoyant portion. Then, we find that the growth-rate curve p roughly verifies:

$$p \approx \gamma + \frac{(\rho_1 - \rho_2)\, h_1 g}{2\eta_1} = 8.5 \times 10^{-15}\ \text{s}^{-1} \approx 1/3.5\ \text{Ma}.$$

This last equality implies that when the lower and dense section of the upper mantle is coupled to its upper buoyant part, lithospheric destabilization requires several few tens of Ma. Such values are very similar to those derived in other models accounting for a power-law rheology (Pierce & Morgan 1992; Meissner & Mooney 1998; Schott & Schmeling 1998; Neil & Houseman 1999; Elkins-Tanton 2007; Molnar & Houseman 2013). We clearly see that if the dense part of the lithosphere is coupled to its buoyant part, there is no way to predict a delamination of the Wyoming lithosphere at similarly fast rates as observed. Obviously, when the dense and buoyant parts are disconnected the major restrictive condition for a fast delamination is that the rheology of the lithosphere is perfectly plastic (i.e. $n = \infty$). It is then the magnitude of the asthenospheric viscosity that

controls whether delamination is fast or slow. Actually, if we assume that $\eta_2 = 10^{18}$ Pa s, we see that the amplitude of the delamination instability increases by a factor $\exp(15) = \sim 3 \times 10^6$ in about 10^5 yr; if we take $\eta_2 = 10^{20}$ Pa s which is probably a maximum estimate for an asthenospheric viscosity below the Western USA (Section 2), the amplitude of the delamination instability increases by a factor $\exp(4.5) = \sim 100$ after 3 Ma. During that time, the Yellowstone plume migrates northeast by ∼60 km, a distance sufficiently important to deflect the plume, a fact which is clearly not observed. Thus, we conclude that the upper bound for asthenospheric viscosity allowing fast delamination of the Wyoming lithosphere is $\eta_2 = 10^{19}$ Pa s, which is in good agreement with estimates derived from post-glacial rebound data in the Western USA (Section 2).

The arguments considered here do not depend on the azimuth around the plume axis. For instance seismic reflectors at ∼100 km depth, which are indicative of a decoupling of the lower part of the lithosphere by magmatic sills are also observed across southeast and northwest profiles intersecting the axis of the Yellowstone plume (Yuan *et al.* 2010). Accordingly, the whole Wyoming lithosphere at the east of the Yellowstone plume may delaminate with a horizontal wavelength of ∼170 km for the detached dense pieces of lithosphere deduced from the present stability analysis, in good agreement with the curvature radius of the seismic parabola around Yellowstone (Figs 1 and 2). As observed along different SE and NW profiles across the YSRP, the enlargement of the seismic parabola to the southwest indicates that the delamination of the Wyoming lithosphere does not stop after the northeast shift of the Yellowstone plume. Again, this fact must be a consequence of the stretching of the Wyoming lithosphere, which itself essentially results from the lithosphere/asthenosphere density contrast at 100–200 km depth. Therefore, along the direction parallel to the ESRP, the delamination front must follow the plume trajectory, whereas, along its orthogonal directions, the propagation front must follow the limit of the seismic parabola. Note that the plume - cratonic lithosphere configurations below the C-volcanic region and below the YC are very similar (Fig. 1b). This leads to propose that the northwest enlargement of the seismic parabola results from the cratonic delamination triggered by the 'C-mantle plume'.

In a recent paper, Burov & Gerya (2014) studied stretching instabilities generated by a plume under a continental mantle decoupled from its overlying crust. They consider the instabilities generated by plate extension or/and by the impingement of a mantle plume at the base of the lithosphere. They accounted for self-consistent non-Newtonian power-law visco-plastic rheology similar to our (3) and (4). They assumed initial values of $C = 20$ MPa for cohesion and $\phi = 30^\circ$ for friction angle implying high yield stresses for the onset of failure. However, they also accounted for strain weakening with $C = 3$ MPa and $\phi = 0^\circ$ at shear-strain greater than 25 per cent, thus drastically reducing lithospheric strength with time. Unfortunately Burov & Gerya (2014) do not display strength envelops nor integrated stresses within their lithosphere. Based on previous models by Burov & Guillou-Frottier (2005), an upper bound of 100 MPa is likely to characterise the mean strength of the lithosphere of Burov & Gerya (2014). They also accounted for slow background stretching rates of $\sim 6 \times 10^{-17}$ s^{-1} (3 mm yr^{-1} applied over a model length size of 1500 km). Accordingly here, the maximum effective viscosity is 1.5×10^{24} Pa s and at 6×10^{24} Pa s whether we assume a mean lithospheric strength of 100 MPa (Burov & Guillou-Frottier 2005) or 400 MPa (Regenauer-Lieb *et al.* 2008), that is, corresponding to the upper range of values considered in our alternative model (Fig. 7).

Our last case (f) in Fig. 7, with $\gamma = 6 \times 10^{-17}$ s^{-1}, $\eta_1 = 8 \times 10^{23}$ Pa s, and $\eta_2 = 10^{18}$ Pa s, provides the greatest growth rate, since stretching instabilities grow with increasing background strain-rate (γ), with increasing lithospheric viscosity (η_1), and with decreasing asthenospheric viscosity (η_2). This growth rate represents a dimensional value of 1.2×10^{-10} s^{-1} (∼1/200 yr). Note that Burov & Gerya (2014) accounted for a minimum viscosity η_2 ranging between 10^{19} Pa s and 10^{20} Pa s. Accordingly, the growth rate of their stretching instability ranges between 1/2000 yr and 1/20 000 yr. Their model displays concentric waves with a wavelength ranging between 150 km and 250 km at time 200 ka, that is, ten times greater than our minimum estimation of the growth rate. Thus, such results agree perfectly with our simple stability analysis, despite our assumptions of a free-slip top boundary and layered constant viscosities.

4 A PLUME MODEL

We investigate the 3-dimensional convection pattern under the YSRP by numerical simulations representing the thermal and flow fields from the Moho down to the bottom of the upper mantle. Fig. 8 displays the 3-D steady temperature field inside our final mantle plume model, and Fig. 9 displays the dynamical flow, the shear and the Bouguer's gravity anomalies (details of the numerical methods, state equations, parameter values and validation of the observed flows and thermal structures are given in Appendix A3). Modelled temperatures at the base of the 'lithosphere', here at 90 km depth below the surface (∼3 GPa) are reported in Fig. 8(h). The maximum temperature close to the plume axis reaches 1510 °C, that is, extremely close to the reported mantle solidus temperature of 1500 °C at 3 GPa (Robinson & Wood 1998). Moreover, the mean value along this horizon is 1340 °C, that is, close to the 1300 °C temperature estimate at the base of continents (Griffin *et al.* 2009). Fig. 8(g) represents the temperature field at the base of the upper low viscosity layer, that is, 150 km depth below the surface (5 GPa). At this depth, the temperature at the axis of our modelled plume is 1655 °C and overlaps with the solidus of garnet-peridotite lithology at 1640 °C (Walter 1998). Between depths 90–150 km, the solidus exceeds by at most 70 °C the temperature along the axis of the plume (Fig. 8f). Assuming a latent heat of crystallization of 500 J g^{-1}, we deduce that, along the axis of the plume, partial melting reached at most ∼20 per cent (Ueki & Iwamori 2013). During early melting, melt forms interstitial films wrapping the solid grains. Such process likely decreases the viscosity of the mantle (Kelemen *et al.* 1997). After partial melting degrees pass afew percent, melt segregates from the solid matrix and concentrates into porous flow channels, dykes or magma pockets, while the several percent of interstitial melt allowing for rheological softening is preserved in the rocks (Rabinowicz & Toplis 2009). It is deduced that, between depths 90–150 km, melt concentration in the mantle is sufficient to maintain a low viscosity horizon and the extra volume of melt produced during decompression is likely transported via dykes into the lithosphere. *A posteriori*, these facts justify the introduction of a 60 km thick layer with a viscosity of 1.5×10^{18} Pa s in our model (see Appendix A3). Also, the hypothesis that the mantle forming this low viscosity 'horizon' contains several percent of interstitial melt could explain why the low velocity zone below the YSRP in Obrebski *et al.*'s (2011) tomographic model is so wide and deep. The mean temperature along the 410-km phase change is 1520 °C, which is a reasonable estimate of the mean mantle temperature at the olivine-spinel transition zone (Katsura & Ito 1989). Finally, the

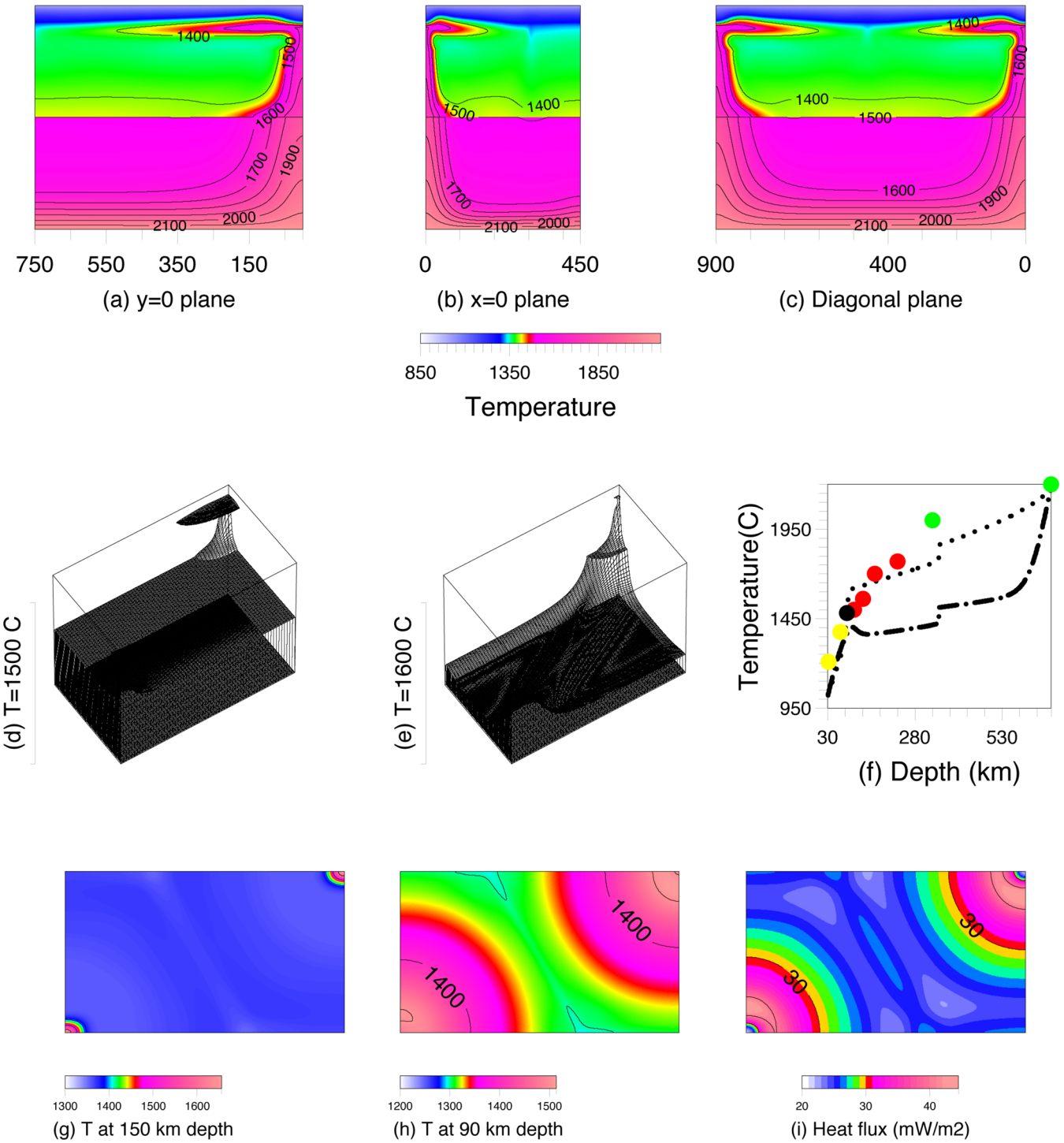

Figure 8. Plume model. In (a), (b) and (c) are drawn the temperature fields along the $x = 0$, $y = 0$ and along the diagonal vertical plane of the computational box, respectively. (d) and (e) are 3-D views of the 1500 °C and 1600 °C isotherms, respectively. In (f) are drawn the mean temperature profile (in dashed line) and the temperature along the axis plume of the model (in dotted line). The solidus down to spinel-garnet transition (80–90 km depth, circles in yellow) is from Hirschmann (2000), the value at the transition (circle in black) is from Robinson & Wood (1998), the solidus within the garnet field (i.e. down to 350 km depth, circles in red) is from Walter (1998) and the solidus through the transition zone (410–660 km depth, circles in green) is from Iwamori (2004). Panels (g) and (h) are the modeled temperuture fields at 150 km depth and 90 km depth, respectively and panel (i) represents the subcrustal heat flow.

temperature at the bottom of the upper mantle is 2150 °C, that is, 50 °C lower than the solidus of peridotitic assemblages estimated by Iwamori (2004).

At depth, convection favours the development of couples of rolls with axes parallel to the x- and y-directions. Due to the viscosity decrease with depth, the ascending flows concentrate and form plumes (Rabinowicz *et al.* 1990). The latter explains the unusual elliptic shape of the hot plume heads (Figs 8d and e). Conversely, dipping flows are sluggish and concentrate into thick vertical planes. The mean heat flux transported by convective flow is 27 mWm^{-2}

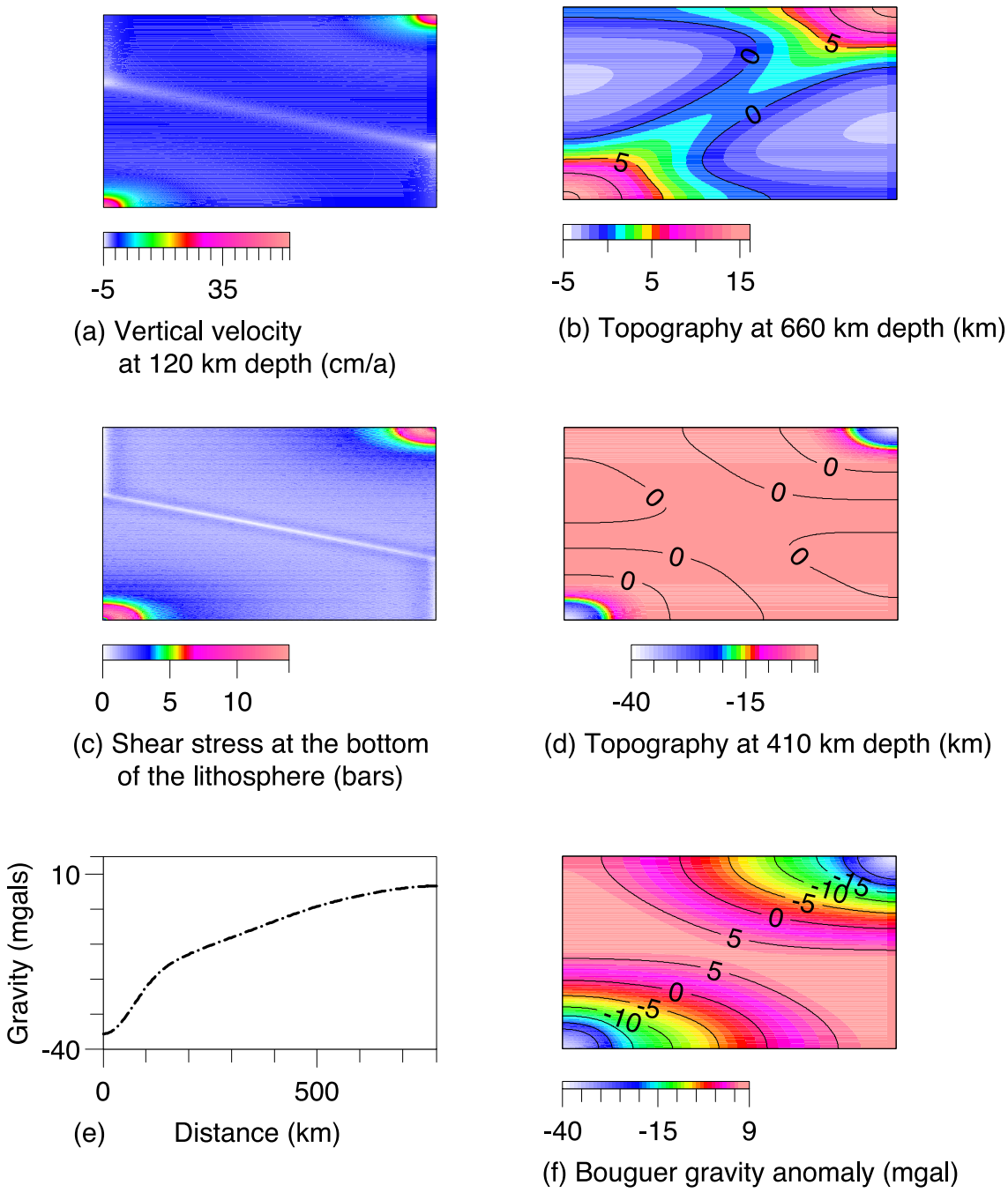

Figure 9. Dynamical quantities of the plume model. (a) the vertical velocity in the middle of the partially molten layer below the lithosphere at 120 km depth; (b) the topography of the 660-km depth discontinuity (positive values indicate positive elevation of the interface); (c) the horizontal shear in bars (1 bar = 0.1 MPa) at the bottom of the lithosphere; (d) topography of the 410-km depth discontinuity (positive values indicate positive elevation of the interface); (e) Bouguer anomaly profile along the long side of the computational box, negative values are found above the axis of the plume; (f) Bouguer anomaly generated by the convective flow, which represents the sum of the gravity anomaly due to the lateral variations of temperature and the deformation of the 410- and the 660-km depth discontinuities, respectively.

(Fig. 8i). Assuming that the radiogenic heat of the crust represents ∼30 to ∼40 mWm^{-2}, we obtain a maximum surface heat flux of 70 mWm^{-2}, a reasonable estimate for a Phanerozoic continent (Jaupart & Mareschal 2007). Nevertheless, this value is half that observed along the Snake River Plain, and three times lower than that of the YC (Smith *et al.* 2009). Such observations indicate that the high heat flux values of the YSRP mainly result from the transient cooling of basaltic intrusions within the crust in the wake of the plume.

Our model reveals two additional particularities, which are scarcely described in other 3-D convective experiments. In the high-viscosity top layer, the temperature is locally low along the ascending axis of the hot plume. The heat flux is actually two times lower than the one several tens of kilometres away from the axis: ∼20 mWm^{-2} instead of ∼40 mWm^{-2} (Figs 8a,b,c and i). Second, we also highlight that temperatures and heat fluxes at the vertical dipping edges of the convecting cells are not minima

(Figs 8b and i). The minima are offset horizontally by ∼100 km inside the convecting cell. These unexpected results must be attributed to the shear along the base of the high viscosity top layer generated by the diverging horizontal flow away from the plume axis. This forced flow transports heat, and further explains the localization of the maximum Moho heat flux ∼100 km away from the axial dipping planes. However, models where high viscosity cold mantle dips towards low viscosity axis of plume can also be obtained by using more realistic rheologies. For instance, 2-D convective experiments with an exponentially decreasing viscosity with temperature display return flows in the high viscosity top layer above ascending and dipping flow, respectively (McKenzie 1977). These flows noticeably modify the stress field and thus the surface topography and gravity, but not the temperature field in the top convective boundary layer. Two-dimensional models with (i) a power-law and temperature-dependent viscosity and (ii) a no-slip top interface, display a cold body tied to the top cold quiescent interface just above the axis of the ascending convective plume (Rabinowicz *et al.* 1980; Christensen 1984). The presence of this cold body leads to a drastic drop of the surface heat flux around the axis of the hot plume which is strongly reminiscent to that observed in the model of Fig. 8 (fig. 1 in Rabinowicz *et al.* 1980). Strikingly, 2-D and 3-D models with rheological laws similar to those used in the latter models but with a top free surface also display the transient generation of a cold body which is still present 1.5 Ma after the collision of a plume with a 150 Ma old tectonic plate (Burov & Guillou-Frottier 2005; Burov & Gerya 2014). Upon arrival of a plume at the bottom of the lithosphere, Burov & Guillou-Frottier (2005) wrote: 'At the first stage, a small-scale domal uplift develops superimposed on large-scale domal uplift (see right column in Fig. 6, wavelength of 300 km). Upon its arrival, the plume head erodes and destabilizes the colder, heavier lithosphere, which develops a Rayleigh–Taylor like instability and sags down. As a result, the plume head is divided onto two diverging zones resulting in the formation of alternating zones of extension and compression in the overlying lithosphere, and hence in two series of zones of uplift and subsidence.' Although we agree with the down sagging of cold mantle at the base of the lithosphere, we believe that its location above the plume axis results from a counter-flow induced by the warm diverging plume flow.

This last result is very important, because it is the stress field generated by the return flows and not the temperature field, which controls the migration of melt throughout the lithosphere. More precisely, because of its weight, the upper part of the cold lithospheric body is in vertical tension (e.g. horizontal compression) while its deeper part is in vertical compression (Fig. 10). Accordingly, the melt, which accumulates at the top of the plume, must migrate via vertically oriented dykes through the deeper part of this cold body. As the tensile direction rotates to horizontal within the body, melt ponds in sills. Finally, the dykes located just on the edges of the plume axis avoid the upper part of the cold body and eventually reach the Moho at some distance away from the plume axis (see Fig. 10). For geometric reasons, it is likely that the Moho domain surrounding the plume axis which cannot be intersected by mantle dykes has a similar horizontal radius than the cold body, that is, ∼50 km in the model of Fig. 8.

5 MODEL PREDICTIONS VERSUS OBSERVATIONS

We illustrate in Fig. 10 the main characteristics of our plume model along the YSRP. The counter-flow in the mantle induces a cold

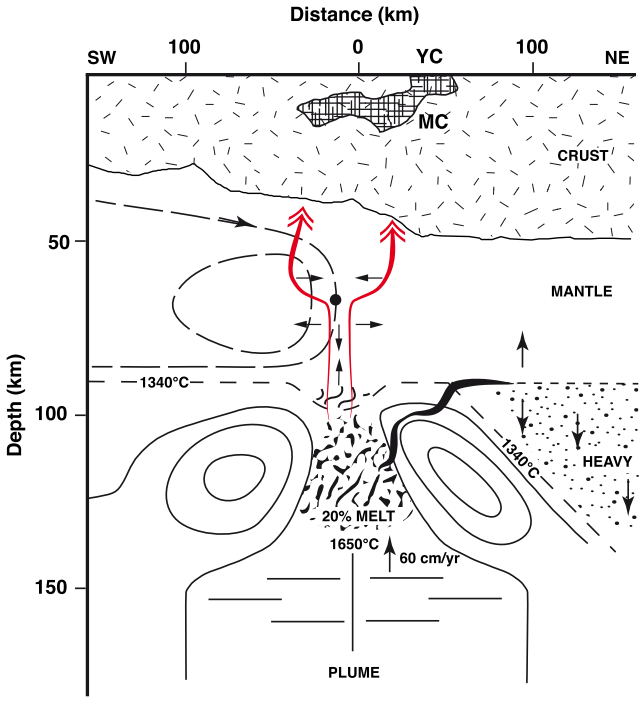

Figure 10. Schematic cartoon along an SW–NE cross-section of the subcontinental structures below YC according to our modelling of the plume and of the destabilization of the Wyoming lithosphere. MC: Magma Chamber whose geometry corresponds to the −2 per cent change of the *P*-wave velocity contour modified from Farrell *et al.* (2014), red arrows indicate the magma flow trajectories (see the text for details).

bulge hanging downwards to the stiff portion of the lithospheric mantle (Figs 8a–c). This bulge is also observed above the plume axis in the tomographic model of Yuan *et al.* (2010) shown in Fig. 3. As described before, at the top of this cold bulge, the induced horizontal compression possibly deviates the melt laterally, which thus percolates along the plume axis to the north and to the south. This explains why the deepest parts of the YC magma chamber plumbing system are located ±50 km away from the plume axis inside the Wyoming craton (Figs 3 and 10; Farrell *et al.* 2014) as also imaged by Huang *et al.* (2015).

The volcanic activity of the Yellowstone area is characterized by abundant rhyolitic eruptions, while the basaltic components remain subordinate (Hildreth *et al.* 1991). Most of these basalts have been largely affected by crustal contamination but the least contaminated ones provide valuable insights on the mantle source. Based on geochemical investigations, Hildreth *et al.* (1991), Graham *et al.* (2009), and Jean *et al.* (2014) proposed that the mantle sources of the Yellowstone basalts do not have a single mantle plume signature but correspond to mixtures of deep plume material, continental lithosphere and shallow asthenospheric mantle. In addition, percolation of melt produced inside the modelled plume a few tens of kilometres upwards through the lower part of the continental lithosphere implies mixing of deep and continental materials in agreement with these geochemical signatures of the Yellowstone basalts.

Within the Wyoming lithosphere, the spinel-garnet phase transition induces a ∼2 per cent increase of the mantle density above 80 km depth (see Appendix A3). This implies that the lower part of the lithosphere is negatively buoyant inducing vertical tension, and consequently, also horizontal compressional stresses. Thus, within the Yellowstone plume, garnet-peridotite partial melting at around 120–150 km depth, within the eastern side of the

plume: (i) migrates upward through dykes, (ii) then penetrates well inside the bulk of the Wyoming craton and (iii) possibly accumulates and recrystallizes inside sills laying in the interface between the dense and buoyant parts of the lithosphere at around 70–90 km depth (Fig. 10). The CCP images of Yuan *et al.* (2010) evidence reflectors at these lithospheric levels with alternative positive and negative polarities corresponding to positive and negative wave velocity gradients, respectively (Fig. 3).

Topographies of the 410- and 660-km discontinuities across the axis of the Yellowstone plume from Sheehan *et al.* (2000) (Fig. 2a) are consistent with those deduced from our numerical model (Figs 9b and d). In our model, the topography of the 660-km discontinuity has a maximum amplitude of 20 km for a half-wavelength of about 280 km, while in Sheehan *et al.* (2000) it is equal to 30 km with a half-wavelength of 150 km at the same order than that imaged by Tauzin *et al.* (2013) with a 0.5° horizontal resolution. The 410-km discontinuity is less constrained, but it is depressed at the plume axis by 50 km at most, whereas our model predicts 40 km (Fig. 9d). Schmandt *et al.* (2012) with large-scale 3-D tomography evidenced a 200-km wide deflection of 18-km amplitude at the 660-km interface consistent with our model, the 410-km interface being difficult to observe.

At larger scale, our model predicts elongated polygonal convective cells. According to the discussion in Section 2.2, 'the rectangle' of vertical hot flows contouring the Yellowstone plume likely represents the evolution of the convective circulation within our model in Fig. 8 after about ∼15 Ma of top-boundary shearing parallel to the plume track (Fig. 2). In particular, 3-D convective experiments with a sheared upper-boundary (e.g. Rabinowicz *et al.* 1990) show that such geometry results from the 'collision' of the Yellowstone plume with the dipping cold flow at its eastern border. Similarly, the proximity of the ascending flow following the SN and the Californian ranges with the cold flow centred below the Eastern California Shear Zone (Fig. 2) may result from eastward relative displacement of the hot flow below the SN and the Californian ranges during the westward shift of the American plate. Because of the alignment of ascending flows along the northern and southern flanks of the seismic parabola, hot plumes become nested in between. Note that the four active volcanoes located directly above the hot area C of Fig. 2 likely represent melt extracted from a plume whose axis of symmetry lies just below the centre of these four volcanoes. Shervais & Vetter (2009) noted that the basaltic volcanism from that area 'underwent an abrupt transition circa ∼700–900 ka from low-K tholeiitic basalt and ferrobasalt to high-K transitional alkali basalt'. Kay & Mahlburg Kay (1993) characterized the geochemical nature of delamination melts as K-rich magmas, which are similar to the high-K alkali basalts from the YSRP. While the two types of basaltic rocks are both related to the activity of the YSRP mantle plume, their contrasting chemical and isotopic signatures evidence that the low-K tholeiitic basalts and ferrobasalts have similar complex mantle sources than their equivalent from the East Snake River Plain including those from Yellowstone, in particular mantle sources implying the mixing of deep plume materials and old continental lithosphere (Hildreth *et al.* 1991; Hanan *et al.* 2008; Shervais & Vetter 2009; Jean *et al.* 2014). In contrast, the younger high-K basalts, which display major elements typical of delamination melts (e.g. Kay & Mahlburg Kay 1993), witness essentially an isotopic deep mantle source of the Yellowstone plume (Jean *et al.* 2014). According to Shervais & Vetter (2009), this abrupt transition at ∼700 ka probably reflects the erosion of pre-existing mantle lithosphere in the wake of the Yellowstone–Snake River plume and they suggested that the abruptness of this transition implies that it may have a 'catastrophic' origin, such as a lithospheric delamination process caused by a Rayleigh–Taylor instability. According to our model, region C (Fig. 2b) is located above a hot plume originating within the 1000-km large and 800-km deep hot root of the Yellowstone plume. This mantle flow may induce the abrupt delamination of the Wyoming lithosphere present at the northern limit of the seismic parabola.

Fig. 4(e) represents our calculation of the isostasic gravity anomaly with the Bouguer anomaly corrected from crustal thickness. It evidences a slow decrease from the SN to 150 km southwest to YC. Then, the negative gravity slope increases leading to a minimum of −120 mGal 100 km northeast to YC well inside the stable part of the Wyoming craton, for example, where crustal thickness reaches a maximum of 55 km. We report in Fig. 4(e) the gravity profile issued from our convective model taking into account the density anomalies due to the temperature field and the deflection of the 410- and 660-km discontinuities. Such profile originates at the axis of the Yellowstone plume and ends further west in proximity of the SN. The fit with the determined isostasic profile is quite good. Actually, our model does not provide an explanation for the strong negative isostatic anomaly observed further east, well inside the Wyoming craton. This minimum is generally associated with an erroneous estimation of the lower crust density over the Wyoming craton, which is thought to be rich in dense material as eclogites (Gorman *et al.* 2002). According to the data of Griffin *et al.* (2004) analysed in Appendix A1, the dense layer explaining the negative gravity anomaly over the Wyoming craton is not located in the lower crust but rather in the lower half of the Wyoming lithosphere (see Appendix A3). The increase in depth of the centre of the dense layer likely amplifies the negative gravity anomaly resulting from the isostatic compensation of such deep-rooted excess of mass. This analysis is supported by Chaves & Ussami (2013) showing that the geoid over the YSRP region is linked, in first approximation, to the velocity contrast between YSRP and the Wyoming craton over a distance of 150 km. Besides, Smith *et al.* (2009) interpolated an NW–SE gravity profile centred on YC using a model of mantle flow associated with the Yellowstone plume with horizontal viscous layers in order to calculate the dynamical topography induced by the plume. Inverting the density distribution in the plume and the dynamical effect of the plume, they optimized the density profile corresponding to the calculated geoid profile. Then, they explained the major part of the profile over a distance of 300 km on either sides of the hotspot. Our gravity analysis is similar to that of Smith *et al.* (2009) in that both predicted gravity profiles are consistent with observations on the west of YSRP, but without the capacity to explain observations outside this domain.

6 SUMMARY AND CONCLUSIONS

Thanks to the recent significant improvement in resolution of tomographic models of the Western USA, conclusions can be drawn on different aspects of mantle convection over a vast region surrounding the YSRP. From the *P*- and *S*-wave models of Obrebski *et al.* (2011), we know that the subducted Farallon slab along the west coast of USA lies over the perovskite transition layer and flows in the upper mantle well beyond the present position of the Yellowstone plume. Such a fact demonstrates that at least between the west coast and Yellowstone, upper-mantle convection is decoupled from that of the lower mantle. Mapping of the 410- and 660-km phase-change depths all around the YSRP reveals that the ascending flows of the convective cell driven by the Yellowstone plume follow a

parallelogram with vertical edges contouring the whole YSRP (Fig. 2b; Eagar *et al.* 2010). Besides, the Yellowstone plume lies at the immediate vicinity of the eastern side of the parallelogram. It implies that the eastern limit of the Yellowstone plume dips along the parabolic border of the 200–250 km thick section of the Wyoming lithosphere (Fig. 2). The western side of that parallelogram follows the SN rims, which is located ∼1000 km away from the axis of the Yellowstone plume, while the return flow associated with the parallelogram of ascending sheets dips east of the SN and the Eastern California Shear Zone (Fig. 2c). By themselves, these results are not surprising because they may simply result from the shear induced by the westward motion of the American continent at ∼2.5 cm yr^{-1}, parallel to the YSRP (Rabinowicz *et al.* 1990). What is more surprising is that the northern and southern hot sheets parallel to the YSRP are close one to the other. This feature, already considered by Schmandt & Humphreys (2010), is shown to be resulting from the probable vertical stratification of upper-mantle viscosity favouring the development of convective modes with wavelength proportional to twice the thickness of the convective layer in one direction and convective modes with wavelengths proportional to twice the thickness of the asthenosphere in the other direction (see the modelling in Section 4).

More local tomographic models bring invaluable information on the detailed structure of the Yellowstone plume. The fast body encased between depths 50 and 90 km, inside the lithosphere, just above the axis of the Yellowstone plume and above the region where the mantle seismic velocities are the slowest (Yuan *et al.* 2010), indicates that a cold counter-flow develops along the axis of the plume. Such counter-flow is present in our plume model of Fig. 8, which takes into account the lithosphere as a highly viscous horizon of constant thickness. This is also observed in 2-D and 3-D models taking into account more complex mantle rheology (Rabinowicz *et al.* 1980; Christensen 1984; Burov & Guillou-Frottier 2005; Burov & Gerya 2014). At the top of this cold and dense body encased inside the lithosphere above the axis of the plume, horizontal compression prevails. This implies that melt percolating from the plume axis is driven around the dense body and ponds few tens of kilometres aside the plume axis (Yuan *et al.* 2010; Farrell *et al.* 2014; Huang *et al.* 2015).

We can extend these last results to the volcanic zone C. Indeed, the analysis of the tomographic model of Section 2.2 strongly suggests that below zone C lays a hot plume encased inside the northern east–west ascending hot sheet of the hot parallelogram contouring the Yellowstone plume. The C plume also roots within the 800 km deep hot horizon. Curiously, the four active volcanoes of region C are distributed at the corner of a 60-km size 'squared' domain. Thus, if we assume that a cold body atop its axis also overlies the C plume, then we can deduce that the four volcanoes simply delimitate a zone where dykes, originated below the lithosphere and inside the plume axis, emerge at the surface. Accordingly, there are at least two upper-mantle hot plumes at the top of the Yellowstone superswell. This is consistent with Davaille (1999) and Matyska & Yuen (2005) who proposed that several hotspots develop at the top of lower-mantle plume.

Finally, Yuan *et al.*'s (2010) tomographic cross-section along the YSRP shows that just to the east of the dense body encased above the axis of the Yellowstone plume, there is a set of quasi-horizontal reflectors, altogether having a length of ∼150 km, which penetrate inside the bulk of the Wyoming Archean lithosphere, at ∼100 km depth (Fig. 3). In Section 4, we showed that the load of the 100–200 km deep dense section of the Wyoming lithosphere generates vertical extensional stresses in a 100 km deep horizon. These stresses stop the upward percolation of melt flowing inside the Yellowstone plume, which eventually ponds as sills within the ∼100 km deep horizon. Such a process is associated with the decoupling of the upper negatively buoyant and dense deep section of the Wyoming lithosphere over a ∼150 km wide horizontal zone located 50 km east of the plume axis (Figs 3 and 10). Assuming that the lower part of the Wyoming lithosphere is purely plastic, we showed that it will delaminate as fragments about ∼150 km wide within less than 300 ka (Section 4). Such a process likely explains why the Yellowstone plume is not deflected between depths 100 and 200 km when it meets the Wyoming lithosphere. Our analysis being invariant by rotation around the plume axis, we infer that our proposed delamination process also accounts for the continuous widening of the observed tectonic parabola moving in the southwestern direction of the YSRP. These results can also be applied to the C plume which lies in proximity of the northern limit of the seismic parabola. Liu & Stegman (2012) suggested that the development of the Columbia River flood basalt followed the 17 Ma old tearing of the Farallon slab. The induced slab gap permits penetration of the hot plumes into the asthenosphere generated over the Yellowstone superswell. We argue that our model explains the delamination of the Wyoming craton along the YSRP from 14 Ma to present. It is worth emphasizing that volcanism originated just to the west of 0.706 line which represents the boundary between Archean terrains and the accreted Phanerozoic continental blocks (e.g. Jean *et al.* 2014). It is likely that 17–14 Ma ago, tensile stresses generated by the Yellowstone plume in the surrounding of that 0.706 line led to the separation of the old and younger continental blocks and then to the generation of the Columbia River flood basalt (Smith *et al.* 2009).

ACKNOWLEDGEMENTS

We are grateful to G. Ceuleneer for interesting discussions and the improvement of the manuscript and to A.M. Cousin for providing the 3-D sketch of Fig. 2(c). We thank W. Shen for providing the 3-D model of the crust in the Western USA, and the Bureau Gravimétrique International (BGI) for providing the gravimetric data. We acknowledge Dave Yuen and an anonymous reviewer in addition to G. Randy Keller's work, who greatly helped to improve the manuscript. The numerical model of the plume, the equations of the destabilization model and the determination of the density profiles are described in the appendix.

REFERENCES

Anderson, D.L., 2005. Large igneous provinces, delamination, and fertile mantle, *Elements,* **1,** 271–275.

Becker, T.W., 2012. On recent seismic tomography for the western United States, *Geochem. Geophys. Geosyst.,* **13,** Q01W10, doi:10.1029/2011GC003977.

Bills, B.G., Adams, K.D. & Wesnousky, S.G., 2007. Viscosity structure of the crust and upper mantle in western Nevada from isostatic rebound patterns of the late Pleistocene Lake Lahontan high shoreline, *J. geophys. Res.,* **112,** B06405, doi:10.1029/2005JB003941.

Bills, B.G., Currey, D.R. & Marshall, G.A., 1994. Viscosity estimates for the crust and upper mantle from patterns of lacustrine shoreline deformation in the Eastern Great Basin, *J. geophys. Res.,* **99,** 22 059–22 086.

Bird, P., 1979. Continental delamination and the Colorado Plateau, *J. geophys. Res.,* **84,** 7561–7571.

Bonvalot, S. *et al.*, 2012. *World Gravity Map,* co-edited by CGMW, BGI, CNES, IRD.

Buehler, J.S. & Shearer, P.M., 2012. Localized imaging of the uppermost mantle with USArray Pn data, *J. geophys. Res.,* **117,** B09305, doi:10.1029/2012JB009433.

Bürgmann, R. & Dresen, G., 2008. Rheology of the lower crust and upper mantle: evidence from rock mechanics, geodesy, and field observations, *Ann. Rev. Earth planet. Sci.,* **36,** 531–567.

Burov, E. & Gerya, T.V., 2014. Asymmetric three-dimensional topography over mantle plumes, *Nature,* **513,** 85–89.

Burov, E. & Guillou-Frottier, L., 2005. The plume head–continental lithosphere interaction using a tectonically realistic formulation for the lithosphere, *Geophys. J. Int.,* **161,** 469–490.

Busse, F.H. *et al.*, 1994. 3D convection at infinite Prandtl number in Cartesian geometry — a benchmark comparison, *Geophys. astrophys. Fluid. Dyn.,* **75,** 39–59.

Camp, V.E., 1995. Mid-Miocene propagation of the Yellowstone mantle plume head beneath the Columbia River basalt source region, *Geology,* **23,** 435–438.

Carlson, R.W., Irving, Schulze, A.J., Carter, D.J. & Hearn, B., Jr., 2004. Timing of Precambrian melt depletion and Phanerozoic refertilization events in the lithospheric mantle of the Wyoming Craton and adjacent Central Plains Orogen, *Lithos,* **77,** 453–472.

Chamberlain, K.R., Frost, C.D. & Frost, B.R., 2003. Early Archean to Mesoproterozoic evolution of the Wyoming Province: Archean origins to modern lithospheric architecture, *Can. J. Earth Sci.,* **40,** 1357–1374.

Chaves, C.A.M. & Ussami, N., 2013. Modeling 3-D density distribution in the mantle from inversion of geoid anomalies: application to the Yellowstone Province, *J. geophys. Res.,* **118,** 6328–6351.

Christensen, U.R., 1984. Heat transport by variable viscosity convection and implications for the Earth's thermal evolution, *Phys. Earth planet. Inter.,* **35,** 264–282.

Chulick, G.S. & Mooney, W.D., 2002. Seismic structure of the crust and uppermost mantle of North America and adjacent oceanic basins: a synthesis, *Bull. seism. Soc. Am.,* **92,** 2478–2492.

Conrad, C.P. & Molnar, P., 1997. The growth of Rayleigh—Taylor-type instabilities in the lithosphere for various rheological and density structures, *Geophys. J. Int.,* **129,** 95–112.

Courtillot, V., Davaille, A., Besse, J. & Stock, J., 2003. Three distinct types of hotspots in the Earth's mantle, *Earth planet. Sci. Lett.,* **205,** 295–308.

Cserepes, L. & Yuen, D.A., 2000. On the possibility of a second kind of mantle plume, *Earth planet. Sci. Lett.,* **183,** 61–71.

Cserepes, L., Rabinowicz, M. & Rosemberg-Borot, C., 1988. Three-dimensional infinite Prandtl number convection in one and two layers with implications for the Earth's gravity field, *J. geophys. Res.,* **93,** 12 009–12 025.

Davaille, A., 1999. Simultaneous generation of hotspots and superswells by convection in a heterogeneous planetary mantle, *Nature,* **402,** 756–760.

DeBremaecker, J.C., 1977. Oceanic lithosphere elastic or viscous, *J. geophys. Res.,* **82,** 2001–2004.

DeCelles, P.G., 2004. Late Jurassic to Eocene evolution of the Cordilleran thrust belt and foreland basin system, western U.S.A., *Am. J. Sci.,* **304,** 105–168.

DeNosaquo, K.R., Smith, R.B. & Lowry, A.R., 2009. Density and lithospheric strength models of the Yellowstone–Snake River Plain volcanic system from gravity and heat flow data, *J. Volc. Geotherm. Res.,* **188,** 108–127.

Duretz, T., May, D.A., Gerya, T.V. & Tackley, P.J., 2011. Discretization errors and free surface stabilization in the finite difference and marker-in-cell method for applied geodynamics: a numerical study, *Geochem. Geophys. Geosyst.,* **12,** Q07004, doi:10.1029/2011GC003567.

Eagar, K.C., Fouch, M.J. & James, D.E., 2010. Receiver function imaging of upper mantle complexity beneath the Pacific Northwest, United States, *Earth planet. Sci. Lett.,* **297,** 140–152.

Elkins-Tanton, L.T., 2007. Continental magmatism, volatile recycling, and a heterogeneous mantle caused by lithospheric gravitational instabilities, *J. geophys. Res.,* **112,** B03405, doi:10.1029/2005JB004072.

English, J.M., Johnston, S.T. & Wang, K., 2003. Thermal modelling of the Laramide Orogeny: testing the flat-slab subduction hypothesis, *Earth planet. Sci. Lett.,* **214,** 619–632.

Farrell, J., Husen, S. & Smith, R.B., 2009. Earthquake swarm and b-value characterization of the Yellowstone volcano-tectonic system, *J. Volc. Geotherm. Res.,* **188,** 260–276.

Farrell, J., Smith, R.B., Husen, S. & Diehl, T., 2014. Tomography from 26 years of seismicity revealing that the spatial extent of the Yellowstone crustal magma reservoir extends well beyond the Yellowstone caldera, *Geophys. Res. Lett.,* **41,** 3068–3073.

Fee, D. & Dueker, K., 2004. Mantle transition zone topography and structure beneath the Yellowstone hotspot, *Geophys. Res. Lett.,* **31,** L18603, doi:10.1029/2004GL020636.

Foley, S.F., 2008. Rejuvenation and erosion of the cratonic lithosphere, *Nat. Geosci.,* **1,** 503–510.

Foster, D.A., Mueller, P.A., Mogk, D.W., Wooden, J.L. & Vogl, J.J., 2006. Proterozoic evolution of the western margin of the Wyoming craton: implications for the tectonic and magmatic evolution of the northern Rocky Mountains, *Canadian J. Earth Sci.,* **43,** 1601–1619.

Foulger, G.R. & Natland, J.H., 2003. Is "hotspot" volcanism a consequence of plate tectonics?, *Science,* **300,** 921–922.

Fourel, L., Milelli, L., Jaupart, C. & Limare, A., 2013. Generation of continental rifts, basins, and swells by lithosphere instabilities, *J. geophys. Res.,* **118,** 3080–3100.

Fukao, Y. & Obayashi, M., 2013. Subducted slabs stagnant above, penetrating through, and trapped below the 660 km discontinuity, *J. geophys. Res.,* **118,** 5920–5938.

Gilbert, H.J., Sheehan, A.F., Dueker, K. & Molnar, P., 2003. Receiver functions in the western United States, with implications for upper mantle structure and dynamics, *J. geophys. Res.,* **108,** 2229, doi:10.1029/2001JB001194.

Goes, S. & van der Lee, S., 2002. Rejuvenation and erosion of the cratonic lithosphere, *J. geophys. Res.,* **107,** 2050, doi:10.1029/2000JB000049.

Gorman, A.R. *et al.*, 2002. Deep Probe: imaging the roots of western North America, *Can. J. Earth Sci.,* **39,** 375–398.

Graham, D.W., Reid, M.R., Jordan, B.T., Grunder, A.L., Leeman, W.P. & Lupton, J.E., 2009. Mantle source provinces beneath the northwestern USA delimited by helium isotopes in young basalts, *J. Volc. Geotherm. Res.,* **188,** 128–140.

Griffin, W.L., O'Reilly, S.Y., Afonso, J.C. & Begg, G.C., 2009. The composition and evolution of lithospheric mantle: a re-evaluation and its tectonic implications, *J. Petrol.,* **50,** 1185–1204.

Griffin, W.L., O'Reilly, S.Y., Doyle, B.J., Pearson, N.J., Coopersmith, H., Kivi, K., Malkovets, V. & Pokhilenko, N., 2004. Lithosphere mapping beneath the North American plate, *Lithos,* **77,** 873–922.

Hacker, B.R. & Abers, G.A., 2004. Subduction Factory 3: an Excel worksheet and macro for calculating the densities, seismic wave speeds, and H_2O contents of minerals and rocks at pressure and temperature, *Geochem. Geophys. Geosyst.,* **5,** Q01005, doi:10.1029/2003GC000614.

Hanan, B.B., Shervais, J.W. & Vetter, S.K., 2008. Yellowstone plume–continental lithosphere interaction beneath the Snake River Plain, *Geology,* **36,** 51–54.

Hildreth, W.E.S., Halliday, A.N. & Christiansen, R.L., 1991. Isotopic and chemical evidence concerning the genesis and contamination of basaltic and rhyolitic magma beneath the Yellowstone Plateau volcanic field, *J. Petrol.,* **32,** 63–138.

Hirschmann, M.M., 2000. Mantle solidus: experimental constraints and the effects of peridotite composition, *Geochem. Geophys. Geosyst.,* **1,** doi:10.1029/2000GC000070.

Hopper, E., Ford, H.A., Fischer, K.M., Lekic, V. & Fouch, M.J., 2014. The lithosphere–asthenosphere boundary and the tectonic and magmatic history of the northwestern United States, *Earth planet. Sci. Lett.,* **402,** 69–81.

Houseman, G.A. & McKenzie, D., 1981. Convective instability of a thickened boundary layer and its relevance for the thermal evolution of continental convergent belts, *J. geophys. Res.,* **86,** 6115–6132.

Houseman, G.A. & McKenzie, D., 1982. Numerical experiments on the onset of convective instability in the Earth's mantle, *Geophys. J. R. astr. Soc.,* **68,** 133–164.

Houseman, G.A. & Molnar, P., 1997. Gravitational (Rayleigh-Taylor) instability of a viscosity and convective thinning of continental layer with non-linear lithosphere, *Geophys. J. Int.,* **128,** 125–150.

Huang, Z. & Zhao, D., 2013. Mapping P-wave azimuthal anisotropy in the crust and upper mantle beneath the United States, *Phys. Earth planet. Inter.,* **225,** 28–40.

Huang, H.-H., Lin, F.-C., Schmandt, B., Farrell, J., Smith, R.B. & Tsai, V.C., 2015. The Yellowstone magmatic system from the mantle plume to the upper crust, *Science,* **348,** 773–776.

Humphreys, E.D., Dueker, K., Schutt, D.L. & Smith, R.B., 2000. Beneath Yellowstone: evaluating plume and nonplume models using teleseismic images of the upper mantle, *GSA Today,* **10,** 1–7.

Husen, S. & Smith, R.B., 2004. Probabilistic earthquake relocation in three-dimensional velocity models for the Yellowstone National Park Region, Wyoming, *Bull. seism. Soc. Am.,* **94,** 880–896.

Ismail-Zadeh, A.T., Huppert, H.E. & Lister, J.R., 2002. Gravitational and buckling instabilities of a rheologically layered structure: implications for salt diapirism, *Geophys. J. Int.,* **148,** 288–302.

Iwamori, H., 2004. Phase relations of peridotites under H2O-saturated conditions and ability of subducting plates for transportation of H2O, *Earth planet. Sci. Lett.,* **227,** 57–71.

Jackson, J. & Blenkinsop, T., 1993. The Malawi earthquake of March 10, 1989 - Deep faulting within the East-African rift system, *Tectonics,* **12,** 1131–1139.

James, T.S., Clague, J.J., Wang, K. & Hutchinson, I., 2000. Postglacial rebound at the northern Cascadia subduction zone, *Quat. Sci. Rev.,* **19,** 1527–1541.

James, D.E., Fouch, M.J., Carlson, R.W. & Roth, J.B., 2011. Slab fragmentation, edge flow and the origin of the Yellowstone hotspot track, *Earth planet. Sci. Lett.,* **311,** 124–135.

Jaupart, C. & Mareschal, J.-C., 2007. Heat flow and thermal structure of the lithosphere, *Treatise on Geophysics,* **6,** 217–251.

Jean, M.M., Hanan, B.B. & Shervais, J.W., 2014. Yellowstone hotspot–continental lithosphere interaction, *Earth planet. Sci. Lett.,* **389,** 119–131.

Johnson, T.E., Brown, M., Kaus, B.J.P. & VanTongeren, J.A., 2014. Delamination and recycling of Archaean crust caused by gravitational instabilities, *Nat. Geosci.,* **7,** 47–52.

Kanamori, H. & Anderson, D.L., 1975. Theoretical basis of some empirical relations in seismology, *Bull. seism. Soc. Am.,* **65,** 1073–1095.

Karato, S., 1997. On the separation of crustal component from subducted oceanic lithosphere near the 660 krn discontinuity, *Phys. Earth planet. Inter.,* **99,** 103–111.

Katsura, T. & Ito, E., 1989. The system Mg_2SiO_4-Fe_2SiO_4 at high pressures and temperatures: precise determination of stabilities of olivine, modified spinel, and spinel, *J. geophys. Res.,* **94,** 15 663–15 670.

Kay, R. & Mahlburg Kay, S., 1993. Delamination and delamination magmatism, *Tectonophysics,* **219,** 177–189.

Kelbert, A., Egbert, G. & deGroot-Hedlin, C., 2012. Crust and upper mantle electrical conductivity beneath the Yellowstone hotspot track, *Geology,* **40,** 447–450.

Kelemen, P.B., Hirth, G., Shimizu, N., Spiegelman, M. & Dick, H.J.B., 1997. A review of melt migration processes in the adiabatically upwelling mantle beneath oceanic spreading ridges, *Phil. Trans. R. Soc. Lond., A.,* **355,** 283–318.

Kincaid, C., Druken, K.A., Griffiths, R.W. & Stegman, D.R., 2013. Bifurcation of the Yellowstone plume drivan by subduction-induced mantle flow, *Nat. Geosci.,* **6,** 395–399.

King, S.D. & Anderson, D.L., 1995. An alternative mechanism of flood basalt formation, *Earth planet. Sci. Lett.,* **136,** 269–279.

Kuntz, M.A., Covington, H.R. & Schorr, L.J., 1992. An overview of basaltic volcanism of the eastern Snake River Plain, Idaho, in *Regional Geology of Eastern Idaho and Western Wyomin,* pp. 227–267, eds Link, P.K., Kuntz, M.A. & Platt, L.B., Mem. Geol. Soc. Am.

Kusky, T.M., Windley, B.F., Wang, L., Wang, Z., Li, X. & Zhu, P., 2014. Flat slab subduction, trench suction, and craton destruction: comparison of the North China, Wyoming, and Brazilian cratons, *Tectonophysics,* **630,** 208–221.

Lee, C.-T.A. & Chen, W.-P., 2007. Possible density segregation of subducted oceanic lithosphere along a weak serpentinite layer and implications for compositional stratification of the Earth's mantle, *Earth planet. Sci. Lett.,* **255,** 357–366.

Leeman, W.P., Schutt, D.L. & Hughes, S.S., 2009. Thermal structure beneath the Snake River Plain: implications for the Yellowstone hotspot, *J. Volc. Geotherm. Res.,* **188,** 57–67.

Levander, A. & Miller, M.S., 2012. Evolutionary aspects of lithosphere discontinuity structure in the western U.S., *Geochem. Geophys. Geosyst.,* **13,** Q0AK07, doi:10.1029/2012GC004056.

Liao, J., Gerya, T.V. & Wang, Q., 2013. Layered structure of the lithospheric mantle changes dynamics of craton extension, *Geophys. Res. Lett.,* **40,** 5861–5866.

Liu, L., Spasojevic, S. & Gurnis, M., 2008. Reconstructing farallon plate subduction beneath North America back to the late cretaceous, *Science,* **322,** 934–938.

Liu, L. & Stegman, D.R., 2011. Segmentation of the Farallon slab, *Earth planet. Sci. Lett.,* **311,** 1–10.

Liu, L. & Stegman, D.R., 2012. Origin of Columbia River flood basalt controlled by propagating rupture of the Farallon slab, *Nature,* **482,** 386–389.

Livaccari, R.F. & Perry, F.V., 1993. Isotopic evidence for preservation of lithospheric mantle during the Sevier–Laramide orogeny, western U.S., *Geology,* **21,** 719–722.

Mambole, A. & Fleitout, L., 2002. Petrological layering induced by an endothermic phase transition in the Earth's mantle, *Geophys. Res. Lett.,* **29,** 2044, doi:10.1029/2002GL014674.

Matyska, C. & Yuen, D.A., 2005. The importance of radiative heat transfer on superplumes in the lower mantle with the new post-perovskite phase change, *Earth planet. Sci. Lett.,* **234,** 71–81.

McCaffrey, K.J.W., King, R.W., Payne, S.J. & Lancaster, M., 2013. Active tectonics of northwestern U.S. inferred from GPS-derived surface velocities, *J. geophys. Res.,* **118,** 709–723.

McKenzie, D., 1977. Surface deformation, gravity anomalies and convection, *Geophys. J. R. astr. Soc.,* **48,** 211–238.

McKenzie, D., Roberts, J.M. & Weiss, N.O., 1974. Convection in the earth's mantle: towards a numerical simulation, *J. Fluids Mech.,* **62,** 465–538.

Meissner, R. & Mooney, W.D., 1998. Weakness of the lower continental crust: a condition for delamination, uplift, and escape, *Tectonophysics,* **296,** 47–60.

Miller, M.S. & Levander, A., 2009. Receiver function images of the Western U.S. lithosphere, *Earthscope OnSite Newsletter,* **4,** 2–3.

Mitrovica, J.X. & Forte, A.M., 2004. A new inference of mantle viscosity based upon joint inversion of convection and glacial isostatic adjustment data, *Earth planet. Sci. Lett.,* **225,** 177–189.

Molnar, P. & Houseman, G.A., 2013. Rayleigh–Taylor instablity, lithospheric dynamics, surface topography at convergent mountain belts, and gravity anomaly, *J. geophys. Res.,* **118,** 2544–2557.

Morency, C. & Doin, M.-P., 2004. Numerical simulations of the mantle lithosphere delamination, *J. geophys. Res.,* **109,** B03410, doi:10.1029/2003JB002414.

Neil, E.A. & Houseman, G.A., 1999. Rayleigh–Taylor instability of the upper mantle and its role in intraplate orogeny, *Geophys. J. Int.,* **138,** 89–107.

O'Reilly, S.Y. & Griffin, W.L., 2010. The continental lithosphere–asthenosphere boundary: can we sample it?, *Lithos,* **120,** 1–13.

Obrebski, M., Allen, R.M., Pollitz, F. & Hung, S.-H., 2011. Lithosphere-asthenosphere interaction beneath the western United States from the joint inversion of body-wave traveltimes and surface-wave phase velocities, *Geophys. J. Int.,* **185,** 1003–1021.

Obrebski, M., Allen, R.M., Xue, M. & Hung, S.-H., 2010. Slab-plume interaction beneath the Pacific Northwest, *Geophys. Res. Lett.,* **37,** L14305, doi:10.1029/2010GL043489.

Parsons, T., Thompson, G.A. & Smith, R.P., 1998. More than one way to stretch: a tectonic model for extension along the plume track of the Yellowstone hotspot and adjacent Basin and Range Province, *Tectonics,* **17,** 221–234.

Pavlis, G.L., Sigloch, K., Burdick, S., Fouch, M.J. & Vernon, F.L., 2012. Unraveling the geometry of the Farallon plate: synthesis of three-dimensional imaging results from USArray, *Tectonophysics,* **532-535,** 82–102.

Payne, S.J., McCaffrey, R., King, R.W. & Kattenborn, S.A., 2012. A new interpretation of deformation rates in the Snake River Plain and adjacent basin and range regions based on GPS measurements, *Geophys. J. Int.,* **189,** 101–122.

Pickering White, B.J., Smith, R.B., Husen, S., Farrell, J. & Wong, I., 2009. Seismicity and earthquake hazard analysis of the Teton-Yellowstone region, Wyoming, *J. Volc. Geotherm. Res.,* **188,** 277–296.

Pierce, K.L. & Morgan, L.A., 1992. The track of the Yellowstone hot spot: volcanism, faulting, and uplift, in *Regional Geology of Eatern Idaho and Western Wyoming,* eds Link, P.K., Kuntz, M.A. & Platt, L. B., Geological Society of America Memoir.

Pierce, K.L. & Morgan, L.A., 2009. Is the track of the Yellowstone hotspot driven by a deep mantle plume? - Review of volcanism, faulting, and uplift in light of new data, *J. Volc. Geotherm. Res.,* **188,** 1–25.

Pollitz, F.F., 2003. Transient rheology of the uppermost mantle beneath the Mojave Desert, California, *Earth planet. Sci. Lett.,* **215,** 89–104.

Porritt, R.W., Allen, R.M. & Pollitz, F.F., 2014. Seismic imaging east of Rocky Mountains with USArray, *Earth planet. Sci. Lett.,* **402,** 16–25.

Poudjom Djomani, Y.H., O'Reilly, S.Y., Griffin, W.L. & Morgan, P., 2001. The density structure of subcontinental lithosphere through time, *Earth planet. Sci. Lett.,* **184,** 605–621.

Prager, W. & Hodge, P.G., 1951. *Theory of Perfectly Plastic Solids*. John Wiley and Sons Inc.

Rabinowicz, M., Calvet, M. & Toplis, M., 2012. Possible layering of mantle convection at the top of the Iceland Hotspot: a crosscheck between 3-D numerical models and gravimetric, seismic and petrological data, *Geophys. J. Int.,* **188,** 35–60.

Rabinowicz, M., Ceuleneer, G., Monnereau, M. & Rosemberg, C., 1990. Three-dimensional models of mantle flow across a low-viscosity zone: implications for hotspot dynamics, *Earth planet. Sci. Lett.,* **99,** 170–184.

Rabinowicz, M., Lago, B. & Froidevaux, C., 1980. Thermal transfer between the continental asthenosphere and the oceanic subducting lithosphere: its effect on subcontinental convection, *J. geophys. Res.,* **85,** 1839–1853.

Rabinowicz, M. & Toplis, M., 2009. Melt Segregation in the lower part of the partially molten mantle zone beneath an oceanic spreading centre: numerical modelling of the combined effects of shear segregation and compaction, *J. Petrol.,* **50,** 1071–1106.

Regenauer-Lieb, K., Rosenbaum, G. & Weinberg, R.F., 2008. Strain localisation and weakening of the lithosphere during extension, *Tectonophysics,* **458,** 96–104.

Ricard, Y., Vigny, C. & Froidevaux, C., 1989. Mantle heterogeneities, geoid, and plate motion: a Monte Carlo inversion, *J. geophys. Res.,* **94,** 13 739–13 754.

Richter, F.M. & Johnson, C.E., 1974. Stability of a chemically layered mantle, *J. geophys. Res.,* **79,** 1635–1639.

Richter, F.M. & Daly, S.F., 1978. Convection models having a multiplicity of large horizontal scales, *J. geophys. Res.,* **83,** 4951–4956.

Robinson, J.A.C. & Wood, B.J., 1998. The depth of the spinel to garnet transition at the peridotite solidus, *Earth planet. Sci. Lett.,* **164,** 277–284.

Roth, J.B., Fouch, M.J., James, D.E. & Carlson, R.W., 2008. Three-dimensional seismic velocity structure of the northwestern United States, *Geophys. Res. Lett.,* **35,** L15304, doi:10.1029/2008GL034669.

Saunders, A.D., Jones, S.M., Morgan, L.A., Pierce, K.L., Widdowson, M. & Xu, Y.G., 2007. Regional uplift associated with continental large igneous provinces: the roles of mantle plumes and the lithosphere, *Chem. Geol.,* **241,** 282–318.

Schmandt, B., Dueker, K., Humphreys, E.D. & Hansen, S., 2012. Hot mantle upwelling across the 660 beneath Yellowstone, *Earth planet. Sci. Lett.,* **331–332,** 224–236.

Schmandt, B. & Humphreys, E.D., 2010. Complex subduction and small-scale convection revealed by body-wave tomography of the western United States upper mantle, *Earth planet. Sci. Lett.,* **297,** 435–445.

Schott, B. & Schmeling, H., 1998. Delamination and detachment of a lithospheric root, *Tectonophysics,* **296,** 225–247.

Schubert, G., Yuen, D.A. & Turcotte, D.L., 1975. Role of Phase Transitions in a Dynamic Mantle, *Geophys. J. Int.,* **42,** 705–735.

Schutt, D.L. & Dueker, K., 2008. Temperature of the plume layer beneath the Yellowstone hotspot, *Geology,* **36,** 623–626.

Schutt, D.L., Dueker, K. & Yuan, H., 2008. Crust and upper mantle velocity structure of the Yellowstone hot spot and surroundings, *J. geophys. Res.,* **113,** B03310, doi:10.1029/2007JB005109.

Sheehan, A.F., Shearer, P.M., Gilbert, H.J. & Dueker, K., 2000. Seismic migration processing of P-SV converted phases for mantle discontinuity structure beneath de Snake River Plain, western United States, *J. geophys. Res.,* **105,** 19 055–19 065.

Shelly, D.R., Hill, D.P., Massin, F., Farrell, J., Smith, R.B. & Taira, T., 2013. A fluid-driven earthquake swarm on the margin of the Yellowstone caldera, *J. geophys. Res.,* **118,** 4872–4886.

Shen, W., Ritzwoller, M.H. & Schulte-Pelkum, V., 2013. A 3-D model of the crust and uppermost mantle beneath the Central and Western US by joint inversion of receiver functions and surface wave dispersion, *J. geophys. Res.,* **118,** 262–276.

Shervais, J.W. & Hanan, B.B., 2008. Lithospheric topography, tilted plumes, and the track of the Snake River-Yellowstone hot spot, *Tectonics,* **27,** TC5004, doi:10.1029/2007TC002181.

Shervais, J.W. & Vetter, S.K., 2009. High-K alkali basalts of the Western Snake River Plain (Idaho): abrupt transition from tholeiitic to mildly alkaline plume-derived basalts, *J. Volc. Geotherm. Res.,* **188,** 141–152.

Sigloch, K., 2011. Mantle provinces under North America from multifrequency *P* wave tomography, *Geochem. Geophys. Geosyst.,* **12,** Q02W08, doi:10.1029/2010GC003421.

Sigloch, K. & Mihalynuk, M.G., 2013. Intra-oceanic subduction shaped the assembly of Cordilleran North America, *Nature,* **496,** 50–57.

Smith, R.B. *et al.*, 2009. Geodynamics of the Yellowstone hotspot and mantle plume: seismic and GPS imaging, kinematics, and mantle flow, *J. Volc. Geotherm. Res.,* **188,** 26–56.

Spada, G., Sabadini, R., Yuen, D.A. & Ricard, Y., 1992. Effects on post-glacial rebound from the hard rheology in the transition zone, *Geophys. J. Int.,* **109,** 683–700.

Stachnik, J.C., Dueker, K., Schutt, D.L. & Yuan, H., 2008. Imaging Yellowstone plume-lithosphere interactions from inversion of ballistic and diffusive Rayleigh wave dispersion and crustal thickness data, *Geochem. Geophys. Geosyst.,* **9,** Q06004, doi:10.1029/2008GC001992.

Tackley, P., 1993. Effects of strongly temperature-dependent viscosity on time-dependent, 3-dimensional models of mantle convection, *Geophys. Res. Lett.,* **20,** 2187–2190.

Tang, Y.-J., Zhang, H.-F., Ying, J.-F. & Su, B.-X., 2013. Widespread refertilization of cratonic and circum-cratonic lithospheric mantle, *Earth-Sci. Rev.,* **118,** 45–68.

Tauzin, B., van der Hilst, R.D., Wittlinger, G. & Ricard, Y., 2013. Multiple transition zone seismic discontinuities and low velocity layers below western United States, *J. geophys. Res.,* **118,** 2307–2322.

Thybo, H. & Artemieva, I.M., 2013. Moho and magmatic underplating in continental lithosphere, *Tectonophysics,* **609,** 605–619.

Tian, Y. & Zhao, D., 2012. P-wave tomography of the western United States: insight into the Yellowstone hotspot and the Juan de Fuca slab, *Phys. Earth planet. Inter.,* **200–201,** 72–84.

Tian, Y., Zhou, Y., Sigloch, K., Nolet, G. & Laske, G., 2011. Structure of North American mantle constrained by simultaneous inversion of multiple-frequency *SH*, *SS*, and Love waves, *J. geophys. Res.,* **116,** B02307, doi:10.1029/2010JB007704.

Till, C.B., Grove, T.L., Carlson, R.W., Fouch, M.J., Donnelly-Nolan, J.M., Wagner, L.S. & Hart, W.K., 2013. Depths and temperatures of <10.5 Ma mantle melting and lithosphere-asthenosphere boundary below southern Oregon and northern California, *Geochem. Geophys. Geosyst.,* **14,** 864–879.

Turcotte, D.L. & Schubert, G., 2002. *Geodynamics,* Cambridge Univ. Press.

Ueki, K. & Iwamori, H., 2013. Thermodynamic model for partial melting of

peridotite by system energy minimization, *Geochem. Geophys. Geosyst.,* **14,** 342–366.
Wagner, L.S. & Long, M.D., 2013. Distinctive upper mantle anisotropy beneath the High Lava Plains and Eastern Snake River Plain, Pacific Northwest, USA, *Geochem. Geophys. Geosyst.,* **14,** 4647–4666.
Wagner, L.S., Forsyth, D.W., Fouch, M.J. & James, D.E., 2010. Detailed three-dimensional shear wave velocity structure of the northwestern United States from Rayleigh wave tomography, *Earth planet. Sci. Lett.,* **299,** 273–284.
Wagner, L.S., Fouch, M.J., James, D.E. & Hanson-Hedgecock, S., 2012. Crust and upper mantle structure beneath the Pacific Northwest from joint inversions of ambient noise and earthquake data, *Geochem. Geophys. Geosyst.,* **13,** Q0AN03, doi:10.1029/2012GC004353.
Waite, G.P. & Smith, R.B., 2002. Seismic evidence for fluid migration accompanying subsidence of the Yellowstone caldera, *J. geophys. Res.,* **107,** 2177, doi:10.1029/2001JB000586.
Waite, G.P., Schutt, D.L. & Smith, R.B., 2005. Models of lithosphere and asthenosphere anisotropic structure of the Yelloxstone hot spot from shear wave splitting, *J. geophys. Res.,* **110,** B11304, doi:10.1029/2004JB003501.
Waite, G.P., Smith, R.B. & Allen, R.M., 2006. V_p and V_s structure of the Yellowstone hot spot from teleseismic tomography: evidence for an upper mantle plume, *J. geophys. Res.,* **111,** B04303, doi:10.1029/2005JB003867.
Walter, M.J., 1998. Melting of garnet peridotite and the origin of komatiite and depleted lithosphere, *J. Petrol.,* **39,** 29–60.
Yuan, H. & Dueker, K., 2005. Teleseismic *P*-wave tomogram of the Yellowstone plume, *Geophys. Res. Lett.,* **32,** L07304, doi:10.1029/2004GL022056.
Yuan, H., Dueker, K. & Stachnik, J.C., 2010. Crustal structure and thickness along the Yellowstone hot spot track: evidence for lower crustal outflow from beneath the eastern Snake River Plain, *Geochem. Geophys. Geosyst.,* **11,** Q03009, doi:10.1029/2009GC002787.
Zandt, G. & Humphreys, E.D., 2008. Toroidal mantle flow through the western U.S. slab window, *Geology,* **36,** 295–298.
Zhang, S. & Yuen, D.A., 1995. The influences of lower mantle viscosity stratification on 3D spherical-shell mantle convection, *Earth planet. Sci. Lett.,* **132,** 157–166.
Zhang, S. & Yuen, D.A., 1996. Various influences on plumes and dynamics in time-dependent, compressible mantle convection in 3-D spherical shell, *Phys. Earth planet. Inter.,* **94,** 241–267.
Ziberna, L., Klemme, S. & Nimis, P., 2013. Garnet and spinel in fertile and depleted mantle: insights from thermodynamic modelling, *Contrib. Mineral. Petrol.,* **166,** 411–421.

APPENDIX

A1 Calculation of mantle density profiles

We calculated three density-depth profiles (Fig. A1) within (i) the Yellowstone plume axis, (ii) the averaged plume area and (iii) the Wyoming craton area. Temperature profiles are those drawn in Fig. 8(f) given the temperature along the axis and the horizontally averaged temperature deduced from the numerical plume model (Fig. 8 and Appendix A3). The mean heat flux of our model represents a reduced heat flux of 27 mW m^{-2} (by reduced, we mean the continental heat flux from which the heat sources of the crust have been subtracted), which is about a factor two greater than that in cratonic zones (Jaupart & Mareschal 2007). Accordingly, the temperature profile adopted for the Wyoming craton is the averaged one of Fig. 8(f), but for which the temperature at depth d is that found in the averaged profile at depth $d/2$.

The rock densities at a defined depth (pressure) have been computed using the Excel macro worksheet provided by Hacker & Abers (2004). This program is based on basic thermodynamic relationships and third-order finite strain theory. The program incorporates a database of physical parameters for 52 rock-forming stable minerals at high pressures and temperatures. This worksheet is especially useful, as mineral modes from studied rock types can easily be modified and the computed rock densities are calculated assuming standard solid mixing theories. For our calculations, we used petrological information from a Kimberlite mantle xenolith study to define the stratigraphic composition of the SCLM below the Wyoming craton (Griffin *et al.* 2004). The SCLM lithology at given depth has been calculated with a harzburgite, lherzolite and pyroxenite contributions. A Wyoming lithospheric thickness of 180 km has also been assumed based on Griffin *et al.* (2004). According to these authors, the lithosphere–asthenosphere boundary has the highest pyroxenite content. This highly enriched section represents a layer of enriched mantle on top of the asthenosphere similar to the perisphere. Above the Yellowstone plume, the lithosphere is strongly thermally and probably compositionally affected by the upwelling plume, and is consequently assumed to be an enriched lherzolite. In our model, the deep asthenosphere has been considered as enriched lherzolite in the plume area and depleted lherzolite below the craton. In addition to compositions and pressure (depth) data, our density calculations also depend on the thermal field. Due to the pressure-temperature dependence of phase diagrams, the depths and nature of the spinel to garnet-peridotite transition from the cold craton to the warm mantle plume area are different. We took these phase relations from the calculated phase diagrams of Ziberna *et al.* (2013).

The calculated densities, estimated lithologies, pressures (depths), and temperatures are summarized in Tables A1a, A1b and A1c, and the final density profiles are drawn in Fig. A1.

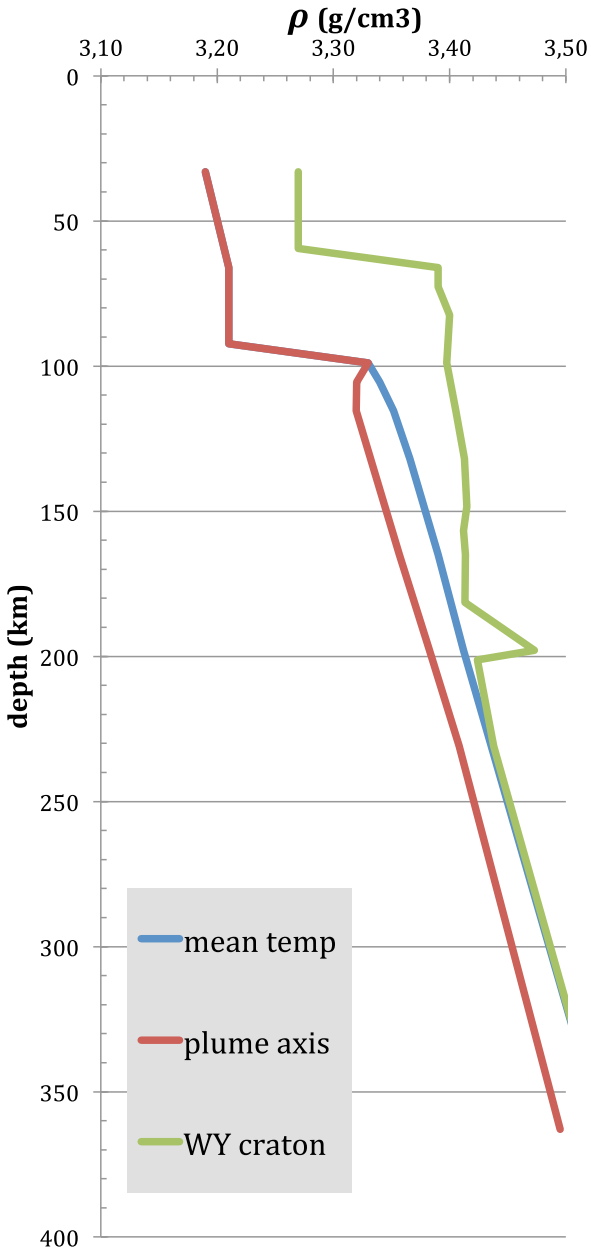

Figure A1. Density profiles.

Table A1a. Parameters used in the mean temperature model.

Depth (km)	Pressure (GPa)	T (°C)	Rock type	% of lithology	ρ (g cm^{-3})
33	1	1000	Spinel lherzolite	100	3.19
66	2	1150	Spinel lherzolite	100	3.21
83	2.5	1300	Spinel lherzolite	100	3.21
92	2.8	1360	Spinel lherzolite	100	3.21
99	3	1420	Garnet lherzolite	100	3.33
106	3.2	1420	Garnet lherzolite	100	3.34
116	3.5	1320	Garnet lherzolite	100	3.35
132	4	1320	Garnet lherzolite	100	3.37
165	5	1350	Garnet lherzolite	100	3.39
198	6	1400	Garnet lherzolite	100	3.41
231	7	1420	Garnet lherzolite	100	3.44
363	11	1450	Garnet lherzolite	100	3.53

Table A1b. Parameters used in the mantle plume axis model.

Depth (km)	Pressure (GPa)	T (°C)	Rock type	% of lithology	ρ (g cm^{-3})
33	1	1000	Spinel lherzolite	100	3.19
66	2	1150	Spinel lherzolite	100	3.21
83	2.5	1300	Spinel lherzolite	100	3.21
92	2.8	1360	Spinel lherzolite	100	3.21
99	3	1420	Garnet lherzolite	100	3.33
106	3.2	1500	Garnet lherzolite	100	3.32
116	3.5	1600	Garnet lherzolite	100	3.32
132	4	1620	Garnet lherzolite	100	3.33
165	5	1660	Garnet lherzolite	100	3.36
198	6	1680	Garnet lherzolite	100	3.38
231	7	1700	Garnet lherzolite	100	3.41
363	11	1875	Garnet lherzolite	100	3.50

Table A1c. Parameters used in the Wyoming craton model.

Depth (km)	Pressure (GPa)	T (°C)	Rock type	% of lithology	ρ (g cm^{-3})
33	1	300	Spinel lherzolite	100	3.27
59	1.8	550	Spinel–garnet lherzolite	100	3.27
66	2	600	Spinel–garnet lherzolite	100	3.39
73	2.2	650	Spinel–garnet lherzolite	100	3.39
83	2.5	700	Spinel–garnet lherzolite	100	3.40
99	3	800	Spinel–garnet lherzolite	100	3.40
116	3.5	850	Spinel–garnet lherzolite	100	3.41
132	4	900	Spinel–garnet lherzolite	100	3.41
149	4.5	1000	Spinel–garnet lherzolite	100	3,42
157	4.8	1050	Garnet lherzolite	25	3.42
157	4,8	1050	Garnet harzburgite	50	3.35
157	4.8	1050	Eclogite	25	3.54
165	5	1100	Garnet lherzolite	25	3.42
165	5	1100	Garnet harzburgite	50	3.35
165	5	1100	Eclogite	25	3.54
182	5.5	1200	Garnet lherzolite	20	3.42
182	5.5	1200	Garnet harzburgite	55	3.35
182	5.5	1200	Eclogite	25	3.55
198	6	1300	Garnet lherzolite	30	3.42
198	6	1300	Garnet harzburgite	20	3.35
198	6	1300	Eclogite	50	3.55
201	6.1	1310	Garnet lherzolite	100	3.42
231	7	1400	Garnet lherzolite	100	3.44
363	11	1450	Garnet lherzolite	100	3.53

A2

The present appendix follows in detail the analytic development that Ismail-Zadeh *et al.* (2002) proposed to compute the growth rate of instabilities due to stretching and diapirism in a plastic layer. Actually, we obtain an expression for the growth rate which differs from the one given in the appendix of Ismail-Zadeh *et al.* (2002). Besides, the tabulation of the growth rate using Ismail-Zadeh *et al.*'s expression does not correspond to the one drawn in their paper, while it agrees with the one presently derived.

In the lithosphere + asthenosphere layer, the basic flow can be approximated to be a pure shear, that is, in 2-D, the horizontal $u(x, z)$ and the vertical $w(x, z)$ velocities both verifying:

$$u(x, z) = \gamma x \tag{A1a}$$

$$w(x, z) = -\gamma z, \tag{A1b}$$

where γ represents the rate of extension of h_1 and h_2 layers underlying the YSRP. Besides, the basic stress field verifies:

$$\tau_{x,x} = -\tau_{z,z} = 2\eta_i \gamma \quad \text{and} \quad \tau_{x,z} = 0. \tag{A2}$$

Because of the development of the shear and diapiric instability, a transient flow $(\tilde{u}(x, z),\ \tilde{w}(x, z))$ develops which induces its own stress field $(\tilde{\tau}_{xx}, \tilde{\tau}_{zz}, \tilde{\tau}_{xz})$. As a first approximation, the stress–strain relationships for this field may be written as (Ismail-Zadeh *et al.* 2002)

$$\tilde{\tau}_{xx} = \frac{2\eta_i}{n}\frac{\partial \tilde{u}}{\partial x}, \quad \tilde{\tau}_{zz} = \frac{2\eta_i}{n}\frac{\partial \tilde{w}}{\partial z}, \quad \tilde{\tau}_{xz} = \eta_i\left(\frac{\partial \tilde{u}}{\partial z} + \frac{\partial \tilde{w}}{\partial x}\right). \tag{A3}$$

In each layer, we have

$$-\frac{\partial}{\partial x}\tilde{P}+\frac{\partial \tilde{\tau}_{xx}}{\partial x}+\frac{\partial \tilde{\tau}_{xz}}{\partial z}=0 \tag{A4a}$$

$$-\frac{\partial}{\partial z}\tilde{P}+\frac{\partial \tilde{\tau}_{xz}}{\partial x}+\frac{\partial \tilde{\tau}_{zz}}{\partial z}=0 \tag{A4b}$$

$$\frac{\partial \tilde{u}}{\partial x}+\frac{\partial \tilde{w}}{\partial z}=0, \tag{A4c}$$

where $\tilde{P}$ designates the effective pressure induced by the transient flow. Using eqs (A3) and (A4c) and multiplying eq. (A4a) by $\frac{\partial^2}{\partial x \partial z}$ and eq. (A4b) by $-\frac{\partial^2}{\partial x^2}$, we obtain

$$\left(\frac{\partial^2}{\partial z^2}-\frac{\partial^2}{\partial x^2}\right)^2 \tilde{w}(z)+\frac{4}{n}\frac{\partial^4 \tilde{w}(z)}{\partial x^2 \partial z^2}=0. \tag{A4d}$$

Let us consider transient flows of the form

$$\tilde{w}(x,z)=\tilde{\tilde{w}}_k(z)\exp(ikx+pt) \tag{A5a}$$

$$\tilde{u}(x,z)=\frac{\partial \tilde{\tilde{w}}_k(z)}{\partial z}\frac{i}{k}\exp(ikx+pt), \tag{A5b}$$

where p represents the growth rate of the instability during time t, k the wavenumber of the perturbation and $\tilde{\tilde{w}}_k(z)$ an eigenfunction of the linear operator:

$$\left(\frac{\partial^2}{\partial z^2}+k^2\right)^2 \tilde{\tilde{w}}(z)-\frac{4k^2}{n}\frac{\partial^2 \tilde{\tilde{w}}(z)}{\partial z^2}=0. \tag{A6}$$

The general solution of this equation when the fluid is Newtonian ($n=1$), that is, in the asthenosphere (Layer 2), $\tilde{\tilde{w}}_k(z)$ writes:

$$\tilde{\tilde{w}}_k(z)=A_2\cosh(kz)+B_2\sinh(kz)+C_2 z\cosh(kz)+D_2 z\sinh(kz). \tag{A7a}$$

In case of a purely plastic lithosphere ($n=\infty$), $\tilde{\tilde{w}}_k(z)$ writes:

$$\tilde{\tilde{w}}_k(z)=A_1\cos(kz)+B_1\sin(kz)+C_1 z\cos(kz)+D_1 z\sin(kz). \tag{A7b}$$

Finally, when the lithosphere has a power-law rheology ($n\neq\infty$ and $n>1$), $\tilde{\tilde{w}}_k(z)$ writes:

$$\begin{aligned}\tilde{\tilde{w}}_k(z)=&\cosh\left(\frac{2kz}{\sqrt{n}}\right)\left(A_1\cos\left(k\sqrt{\frac{n-1}{n}}z\right)+B_1\sin\left(k\sqrt{\frac{n-1}{n}}z\right)\right)\\&+\frac{\sqrt{n}}{2k}\sinh\left(\frac{2kz}{\sqrt{n}}\right)\left(C_1\cos\left(k\sqrt{\frac{n-1}{n}}z\right)+D_1\sin\left(k\sqrt{\frac{n-1}{n}}z\right)\right).\end{aligned} \tag{A7c}$$

It is worthnoting that when n tends to ∞, the expression of $\tilde{\tilde{w}}_k(z)$ given by eq. (A7c) tends to that of eq. (A7b). Parameter values A_1, B_1, C_1, D_1 and A_2, B_2, C_2, D_2 are determined according to the following set of boundary conditions.

The mantle being stiffer in the absence of melt ($\sim 10^{19-20}$ Pa s, instead of 10^{18} Pa s, when it is partially molten; e.g. Rabinowicz *et al.* 2012), we impose a no-slip condition along the bottom of the asthenosphere (Layer 2), here identified as the $\sim$100 km thick zone of partial melting below the Wyoming lithosphere. It implies that

$$\tilde{u}(x,z=-h_2)=\tilde{w}(x,z=-h_2)=0 \Leftrightarrow \tilde{\tilde{w}}_k(z=-h_2)=\frac{\partial \tilde{\tilde{w}}_k(z=-h_2)}{\partial z}=0. \tag{A8a}$$

Similarly, we consider a case where the lower dense section of the Wyoming lithosphere is either decoupled or coupled to its upper buoyant one. In case of coupling, we consider a no-slip condition, while in the decoupled case we adopt a free-slip condition implying that

$$\tilde{w}(x,z=h_1)=\tilde{\tau}_{xz}(x,z=h_1)=0 \Leftrightarrow \tilde{\tilde{w}}_k(z=h_1)=\frac{\partial^2 \tilde{\tilde{w}}_k}{\partial z^2}(z=h_1)=0. \tag{A8b}$$

Along the lithosphere–asthenosphere interface, velocities $\tilde{u}(x,z=0)$ and $\tilde{w}(x,z=0)$ are continuous, that is,

$$\tilde{\tilde{w}}_k^1(z=0)=\tilde{\tilde{w}}_k^2(z=0) \quad \text{and} \quad \frac{\partial \tilde{\tilde{w}}_k^1}{\partial z}(z=0)=\frac{\partial \tilde{\tilde{w}}_k^2}{\partial z}(z=0), \tag{A8c}$$

where $\tilde{\tilde{w}}_k^1$ and $\tilde{\tilde{w}}_k^2$ represent the eigenfunctions of eq. (A6) evaluated in Layer 1 and Layer 2, respectively. Because of the development of the gravitational instability, the interface separating Layer 1 and Layer 2 undulates. Then, height $\xi(x,t)$ above the interface $z=0$ verifies:

$$\xi(x,t)=\xi_0(x)\exp(pt). \tag{A9a}$$

Because

$$\frac{\mathrm{d}\xi\,(x,t)}{\mathrm{d}t} = \tilde{w}_1\,(x, z=0) = \tilde{w}_2\,(x, z=0)\,, \tag{A9b}$$

we deduce that

$$p\xi_0\,(x) = \tilde{\tilde{w}}_k^1\,(z=0) = \tilde{\tilde{w}}_k^2\,(z=0)\,. \tag{A9c}$$

Besides, we assume a first-order approximation of continuity of the total stress tensor driven by the sum of the basic and of the perturbed flows along the vertical and horizontal directions, respectively. As described by Ismail-Zadeh *et al.* (2002), this implies continuity of

$$-\tilde{P}_1\,(z=0) + \tilde{\tau}_{zz,1}\,(z=0) + \rho_1 g\xi\,(x,t) = -\tilde{P}_2\,(z=0) + \tilde{\tau}_{zz,2}\,(z=0) + \rho_2 g\xi\,(x,t) \tag{A10a}$$

and of

$$\tilde{\tau}_{xz,1}\,(z=0) - 2\eta_1\gamma\frac{\partial\xi}{\partial x} = \tilde{\tau}_{xz,2}\,(z=0) - 2\eta_2\gamma\frac{\partial\xi}{\partial x}, \tag{A10b}$$

where g designates the gravity constant, ρ_{i} the density, $\tilde{\tau}_{k,l,i}$ the components of the perturbed stress tensor and $\tilde{P}_i$the dynamical pressure in Layer i, respectively. It is worth noting that $-2\eta_i\gamma\frac{\partial\xi}{\partial x}$ represents the horizontal shear stress resulting from small angle rotation $\frac{\partial\xi}{\partial x}$ of the basic stress field due to the deflection of the $z=0$-interface, while $\tilde{\tau}_{xz,i}\,(z=0)$ represents the shear stress induced by the transient flow field $(\tilde{u}\,(x,z)\,,\,\tilde{w}\,(x,z))$. Derivation of eq. (A10a) by $\frac{\partial}{\partial x}$ leads to

$$-\frac{\partial\tilde{P}_1}{\partial x}(z=0) + \frac{\partial\tilde{\tau}_{zz,1}}{\partial x}(z=0) + \rho_1 g\frac{\partial\xi\,(x,t)}{\partial x} = -\frac{\partial\tilde{P}_2}{\partial x}(z=0) + \frac{\partial\tilde{\tau}_{zz,2}}{\partial x}(z=0) + \rho_2 g\frac{\partial\xi\,(x,t)}{\partial x}. \tag{A10e}$$

In eq. (A10e), we eliminate $\tilde{P}_i$, using eq. (A4a). Finally, using eqs (A3) and (A5), we find that

$$\begin{aligned}&\left(\frac{2\eta_1}{n}\left(-\frac{\partial^2\tilde{u}_1}{\partial x^2} + \frac{\partial^2\tilde{w}_1}{\partial x\partial z}\right) - \eta_1\frac{\partial}{\partial z}\left(\frac{\partial\tilde{u}_1}{\partial z} + \frac{\partial\tilde{w}_1}{\partial x}\right) + \rho_1 g\frac{\partial\xi}{\partial x}\right)(z=0)\\ &\quad= \left(2\eta_2\left(-\frac{\partial^2\tilde{u}_2}{\partial x^2} + \frac{\partial^2\tilde{w}_2}{\partial x\partial z}\right) - \eta_2\frac{\partial}{\partial z}\left(\frac{\partial\tilde{u}_2}{\partial z} + \frac{\partial\tilde{w}_2}{\partial x}\right) + \rho_2 g\frac{\partial\xi}{\partial x}\right)(z=0)\,.\end{aligned} \tag{A10f}$$

Finally, when we derive this last expression with time t, and use eqs (A9), we obtain

$$\left(\eta_1\left(\left(-\frac{4}{n}+1\right)\tilde{\tilde{w}}_k^{1'} + \frac{\tilde{\tilde{w}}_k^{1'''}}{k^2}\right) - \frac{\rho_1 g}{p}\tilde{\tilde{w}}_k^1\right)(z=0) = \left(\eta_2\left(-3\tilde{\tilde{w}}_k^{2'} + \frac{\tilde{\tilde{w}}_k^{2'''}}{k^2}\right) - \frac{\rho_2 g}{p}\tilde{\tilde{w}}_k^2\right)(z=0)\,. \tag{A11a}$$

Similarly, when we derive eq. (A10b) with t, and use eqs (A9), we find that

$$\eta_1\left(-p\left(\frac{\tilde{\tilde{w}}_k^{1''}}{k^2} + \tilde{\tilde{w}}_k^1\right) + 2\gamma\tilde{\tilde{w}}_k^1\right)(z=0) = \eta_2\left(-p\left(\frac{\tilde{\tilde{w}}_k^{2''}}{k^2} + \tilde{\tilde{w}}_k^2\right) + 2\gamma\tilde{\tilde{w}}_k^2\right)(z=0)\,. \tag{A11b}$$

Actually, eq. (A11a) represents flow driven by buoyancy, while eq. (A11b) represents flow driven by shear. As usual, equations are made dimensionless. We introduce the length-scale $h = h_1 + h_2$, and the time-scale $t_0 = 10^{18}$ and 10^{13}s, respectively. Besides, we define the following dimensionless quantities:

$$v = \frac{\eta_2}{\eta_1}, \quad \dot{z} = \frac{z}{h}, \quad \dot{k} = kh, \quad \dot{k}_1 = kh_1, \quad \dot{k}_2 = kh_2, \quad \dot{\tilde{\tilde{w}}}_{\dot{k}}^{\,1} = \frac{\tilde{\tilde{w}}_k^1 t_0}{h}, \quad \dot{\tilde{\tilde{w}}}_{\dot{k}}^{\,2} = \frac{\tilde{\tilde{w}}_k^2 t_0}{h}, \quad \dot{p} = pt_0$$

and

$$G = \frac{(\rho_1 - \rho_2)\,ght_0}{2\eta_1} \quad \text{and} \quad \Gamma = \gamma t_0$$

Actually, G and Γ represent the relaxation rate of buoyancy stresses and total deformation of the lithosphere (Layer 1) during time t_0, respectively. Then, eqs (A11a) and (A11b) write

$$\left(\left(-\frac{4}{n}+1\right)\dot{\tilde{\tilde{w}}}_{\dot{k}}^{\,1'} + \frac{\dot{\tilde{\tilde{w}}}_{\dot{k}}^{\,1'''}}{\dot{k}^2}\right)(\dot{z}=0) = \left(v\left(-3\dot{\tilde{\tilde{w}}}_{\dot{k}}^{\,2'} + \frac{\dot{\tilde{\tilde{w}}}_{\dot{k}}^{\,2'''}}{\dot{k}^2}\right) + \frac{2G}{\dot{p}}\dot{\tilde{\tilde{w}}}_{\dot{k}}^{\,2}\right)(\dot{z}=0) \tag{A12a}$$

and

$$\left(\dot{\tilde{\tilde{w}}}_{\dot{k}}^{\,1} + \frac{\dot{\tilde{\tilde{w}}}_{\dot{k}}^{\,1''}}{\dot{k}^2}\right)(\dot{z}=0) = \left(v\left(\dot{\tilde{\tilde{w}}}_{\dot{k}}^{\,2} + \frac{\dot{\tilde{\tilde{w}}}_{\dot{k}}^{\,2''}}{\dot{k}^2}\right) + \frac{2\Gamma\,(1-v)}{\dot{p}}\dot{\tilde{\tilde{w}}}_{\dot{k}}^{\,2}\right)(\dot{z}=0)\,, \tag{A12b}$$

where $\dot{\tilde{w}}_{\dot{k}}^{1}$ verifies eq. (A7a) and $\dot{\tilde{w}}_{\dot{k}}^{2}$ verifies eqs (A7b) and (A7c), if $n = \infty$ and $n > 1$, respectively. Analytical manipulations of the above set of boundary conditions and of eqs (A12a) and (A12b), applied to the case where the top interface is free-slip and the power-law constant is finite, show that the dimensionless growth rate $\dot{p} = pt_0$ verifies the following couple of equations:

$$\begin{aligned} &A_1\left(a_0\dot{p} + a_1\right) + bC_1 = 0, \\ &A_1\left(c_0\dot{p} + c_1\right) + dC_1 = 0. \end{aligned} \tag{A13a}$$

A non-trivial solution of these equations implies that

$$\dot{p} = \frac{bc_1 - da_1}{a_0 d - c_0 b}, \tag{A13b}$$

where

$$\begin{aligned} a_0 = &\left(dc\left(\frac{5}{2n} - v\right) - v\right)\tan\left(1 - tah^2\right) + \frac{2dc}{n}\sqrt{n-1}\left(\tan^2 + 1\right)\ tah \\ &- \frac{9ua}{2n}\sqrt{\frac{n-1}{n}}\left(1 + (\tan tah)^2\right), \end{aligned} \tag{A13c}$$

$$a_1 = -\tan\left(1 - tah^2\right)\left(\frac{ua}{\dot{k}}G + dc\left(1 - v\right)\Gamma\right), \tag{A13d}$$

$$b = \left(2dc\sqrt{\frac{n-1}{n}}\left(\tan^2 + tah^2\right) + ua\left(\frac{3}{n} - 2\right)\tan\left(1 - tah^2\right) - \frac{9ua}{2\sqrt{n}}\sqrt{\frac{n-1}{n}}tah\left(1 + \tan^2\right)\right), \tag{A13e}$$

$$\begin{aligned} c_0 = &-v\left(dc\sqrt{\frac{n-1}{n}}\left(1 + (\tan tah)^2\right) + \left(ua + 2tah\left(\tilde{k}_2\right)\right)\tan\left(1 - tah^2\right)\right) \\ &- \frac{9\left(dc - tah\left(\dot{k}_2\right)^2\right)}{2n}\sqrt{\frac{n-1}{n}}\left(1 + (\tan tah)^2\right), \end{aligned} \tag{A13f}$$

$$c_1 = -\frac{\left(dc - tah\left(\tilde{k}_2\right)^2\right)\tan\left(1 - tah^2\right)G}{\dot{k}}, \tag{A13g}$$

$$\begin{aligned} d = &\tan\left(1 - tah^2\right)\left(2vdc + \left(\frac{3}{n} - 2\right)\left(dc - tah\left(\dot{k}_2\right)^2\right)\right) \\ &+ tah\left(1 + \tan^2\right)\sqrt{n-1}\left(-\frac{9}{2n}\left(dc - tah\left(\dot{k}_2\right)^2\right) - vdc\right). \end{aligned} \tag{A13h}$$

In the above expressions tan, *tah*, *dc* and *ua* represent the following dimensionless quantities:

$$\tan = \tan\left(\dot{k}_1\sqrt{\frac{n-1}{n}}\right), \quad tah = tah\left(\frac{2\dot{k}_1}{\sqrt{n}}\right), \quad dc = \dot{k}_2{}^2\left(1 - tah\left(\dot{k}_2\right)^2\right), \quad \text{and} \quad ua = \dot{k}_2\left(1 - tah\left(\dot{k}_2\right)^2\right) - tah\left(\dot{k}_2\right).$$

Eq. (A13b) is used to draw Fig. 6 with different viscosity, density contrast and strain-rate values as given in the figure caption. Alternatively, let us consider the case where $n = \infty$, which is then displayed in Fig. 7 for different viscosity, density contrast and strain-rate values. Then:

$$\tan = \tan\left(\dot{k}_1\right) \tag{A14a}$$

$$a_0 = -v\left(dc + 1\right) \tag{A14b}$$

$$a_1 = -\left(\frac{uaG}{\dot{k}} + dc\left(1 - v\right)\Gamma\right) \tag{A14c}$$

$$b = dc\tan - ua \tag{A14d}$$

$$c_0 = -v\left(dc + \left(ua + 2tah\left(\dot{k}_2\right)\right)\tan\right) \tag{A14e}$$

$$c_1 = -\frac{\tan\left(dc - tah\left(\dot{k}_2\right)^2\right)G}{\tilde{k}} \tag{A14f}$$

$$d = -dc\left(\tan\left(1-v\right)+v\dot{k}_1\left(1+\tan^2\right)\right)+\tan\, tah\left(\dot{k}_2\right)^2. \tag{A14g}$$

Actually, coefficients a_0 (eq. A14b) and c_0 (eq. A14e) are proportional to v, while the other coefficients are only weakly modified when setting $v = 0$. More precisely, when we make this approximation, we obtain:

$$p \approx \frac{\sin\left(\dot{k}_1\right)\left(tah^2\left(\dot{k}_2\right)-dc\right)\left(\frac{\sin\left(\dot{k}_1\right)G}{\dot{k}}+\cos\left(\tilde{k}_1\right)\Gamma\right)}{v\left(\sin\left(\dot{k}_1\right)\cos\left(\dot{k}_1\right)\left(dc+tah^2\left(\dot{k}_2\right)\right)+\left(dc-ua-tah^2\left(\dot{k}_2\right)\right)\cos^2\left(\dot{k}_1\right)+\left(ua+2tah\left(\dot{k}_2\right)\right)\sin^2\left(\dot{k}_1\right)\right)}. \tag{A15}$$

This equation shows that the buoyancy term G is proportional to $\frac{\sin\left(\tilde{k}_1\right)}{\tilde{k}}$ and the stretching term Γ to $\cos\left(\tilde{k}_1\right)$. This explains the shape of the curves of Fig. 7.

We have computed the growth-rate curve when $n = \infty$, and by setting a no-slip condition at the top of Layer 1. Those boundary conditions suppose that the deepest and densest section of the lithosphere is pegged to its overlying buoyant part. Then proceeding as above, we find that the growth-rate curve p roughly verifies:

$$\dot{p} \approx \cos^2\left(\tilde{k}_1\right)\Gamma+\left(\tilde{k}_1-\cos\left(\tilde{k}_1\right)\sin\left(\tilde{k}_1\right)\right)G. \tag{A16}$$

This last expression implies that when the wavenumber $\tilde{k}$ is relatively large, p verifies:

$$p \approx \gamma+\frac{\left(\rho_1-\rho_2\right)h_1 g}{2\eta_1}. \tag{A17}$$

A3

We used the convective model and the numerical method presented in Cserepes *et al.* (1988) and which is benchmarked in Busse *et al.* (1994). We consider four superimposed horizontal incompressible fluid layers of constant viscosity with an infinite Prandtl number. Then, the equations of convection in the Boussinesq approximation write:

$$-\vec{\nabla}p'+\eta_i\nabla^2\vec{V}=\alpha\rho g\left(T-T'(z)\right)\vec{e}_z \tag{A18a}$$

$$\vec{\nabla}.\vec{V}=0 \tag{A18b}$$

$$\frac{\partial\left(T-T'(z)\right)}{\partial t}+\vec{V}.\vec{\nabla}\left(T-T'(z)\right)=\kappa\nabla^2\left(T-T'(z)\right). \tag{A18c}$$

The z-axis of the Cartesian coordinate system (x, y, z) points downwards, $\vec{e}_z$ is the corresponding unit vector. The computing box is 640 km high ($z = 0$ at the Moho, i.e. at 30 km depth below the Earth's surface), 750 and 450 km long in the horizontal directions x and y, respectively, η_i is the effective viscosity of the $i = 1$, 2, 3, and 4 horizontal layers, respectively. The top layer ($i = 1$) represents the mantle section of the lithosphere: it is 60 km thick and has a 1.5×10^{23} Pa s viscosity. This latter value is slightly greater than the 5×10^{22} Pa s minimum effective viscosity resulting from the extension rate and the tensile yield in the YSRP (see Section 2). Below it lays the asthenosphere, which is divided into two constant viscosity horizons: the top one ($i = 2$) is 60 km thick and has a viscosity of $\sim 1.5 \times 10^{18}$ Pa s while the bottom one ($i = 3$), which extends from 150 to 410 km depth below the Earth's surface, has a viscosity of 5×10^{19} Pa s (e.g. Rabinowicz *et al.* 2012). Finally, the last layer represents the zone of transition ($i = 4$): it extends from 410 to 670 km depth below the Earth's surface, and has a viscosity of 1.5×10^{21} Pa s (Spada *et al.* 1992). Besides, in above equations: t is the time, $\vec{V} = (u, v, w)$ is the velocity vector, p' the non-hydrostatic pressure, g is the gravity constant (10 m.s^{-2}), $\rho = 3400$ kg m^{-3} represents the mean density of the upper mantle (Poudjom Djomani *et al.* 2001), and $\alpha = 4.510^{-5}$ K^{-1} the mean coefficient of thermal expansion of the mantle (Poudjom Djomani *et al.* 2001), κ the thermal diffusivity of the mantle (here 0.85×10^{-6} m^2 s^{-1}, such value stands for a thermal conductivity $k = 3.6$ Wm^{-1}°K^{-1}, and a specific heat C = 1250 J kg^{-1}°K^{-1}), $T'(z)$ is the adiabatic temperature in the mantle below the crust. To calculate that profile, we assume that (i) the temperature at the Moho interface is 1000 °C, that is, a temperature just greater than 0.9 times the solidus of basaltic rocks and granulites; (ii) the adiabatic gradient is 0.3° km^{-1} through the entire upper mantle; (iii) at 410 km depth, the Clapeyron's slope γ of the olivine/spinel solid phase change is 3 MPa K^{-1} and induces a temperature and a density $\delta\rho$ jump across the phase change interface of 90 K and of 8 per cent (i.e. $\frac{\partial\rho}{\rho} = 0.08$; Schubert *et al.* 1975), respectively. The different quantities introduced here are used to define the Rayleigh number Ra:

$$Ra = \frac{\rho\alpha\Delta T H^3}{\kappa\eta_4}, \tag{A19}$$

where H the height of the upper mantle below the Moho (here 640 km), η_4 is the effective viscosity of the transition zone (here 1.5×10^{21} Pa s) and $\Delta T = 880$ °C is the difference between the absolute temperature imposed at 670 km depth and the adiabatic temperature at the same depth T ($z = 640$ km). Finally, we end with an estimation of the Rayleigh number of 2.5×10^5.

Because of the constant layered viscosity, the velocity field is poloidal around $\vec{e}_z$. Then, the velocity components can be written in terms of the scalar function $U(x, y, z)$ as:

$$u = \frac{\partial^2 U}{\partial x\partial z} \tag{A20a}$$

$$v = \frac{\partial^2 U}{\partial y\partial z} \tag{A20b}$$

$$w = -\left(\frac{\partial^2 U}{\partial x^2} + \frac{\partial^2 U}{\partial y^2}\right). \tag{A20c}$$

Then eliminating the pressure term in eq. (A18a), the equation of motion in each layer i is transformed into:

$$\nabla^4 U = -\frac{\alpha \rho g}{\eta_i}\left(T(x, y, z) - T'(z)\right). \tag{A21}$$

The vertical faces of the computation box are planes of symmetry of the flow. It implies that along the faces orthogonal to the directions $\vec{e}_x$ and $\vec{e}_y$, $\frac{\partial U}{\partial x} = 0$ and $\frac{\partial U}{\partial y} = 0$, respectively. The flow velocities on the top and bottom interfaces of the computation box are null, that is, on these interfaces $U = 0$ and $\frac{\partial^2 U}{\partial z^2} = 0$. The later boundary condition is consistent with a mantle lithosphere globally pegged to the crust (Burov & Guillou-Frottier 2005) and with a lower mantle much more viscous than the upper one (Ricard *et al.* 1989). Finally, we assure continuity of velocities and normal stresses across the different interfaces of the constant viscosity horizons:

$$U_i = U_{i+1}; \quad \frac{\partial U_i}{\partial z} = \frac{\partial U_{i+1}}{\partial z}; \quad \eta_i\left(\frac{\partial^2}{\partial z^2} + 3\left(\frac{\partial^2}{\partial x^2} + \frac{\partial^2}{\partial x^2}\right)\right)\frac{\partial U_i}{\partial z} = \eta_{i+1}\left(\frac{\partial^2}{\partial z^2} + 3\left(\frac{\partial^2}{\partial x^2} + \frac{\partial^2}{\partial x^2}\right)\right)\frac{\partial U_{i+1}}{\partial z}$$

at the common interface between layers i and $i + 1$, respectively.

In the equation of temperature, we neglect the radioactive and shear heating, since both parameters are known to only moderately impact the upper-mantle temperature field (Rabinowicz *et al.* 1980). When the viscosity field presents discontinuities, the account of the shear heating term poses dramatic numerical difficulties (Duretz *et al.* 2011). In our model, the contrast of potential temperature ΔT between the Moho and the 670-km interface is a free parameter. In the present model, we fix $\Delta T = 880\ ^\circ$C, to match a mean horizontal temperature of 1520 $^\circ$C at 410 km depth, that is, at the base of layer $i = 3$. We assume that the heating due to the transformation of spinel into olivine occurs instantaneously. At each time step, during the resolution of the convective equations, the knowledge of the temperature $T_{410}(x,y)$ at 410 km depth allows to calculate the deflection $\Pi(x, y)$ of the olivine-spinel interface. More precisely:

$$\Pi(x, y) = \frac{\gamma\left(T_{410}(x, y) - 1520\ ^\circ\mathrm{C}\right)}{\rho g}, \tag{A22}$$

that is, when a hot plume crosses the interface, the depth of the phase change increases, that is, $\Pi(x, y) > 0$, while in a cold plume it decreases, that is, $\Pi(x, y) < 0$. This deflection being small in comparison with the height of the upper mantle, we assume in our calculation that this interface is straight (McKenzie *et al.* 1974). However, because of the deflection of the olivine-spinel interface, in the hot and cold plumes, the density decreases and increases by $\pm\delta\rho$, in a zone of thickness $\Pi(x, y)$ situated just above and below the phase change horizon, respectively. To take into account of this, after each time step, we compute $\Pi(x, y)$, and then modify the source term of the flow equation through a height corresponding to that of the deflection of the interface. Finally, we compute the deflection of the bottom of the computing box, here the spinel-perovskite interface, evaluating the normal stresses generated by the flow along this interface.

To resolve the temperature equation, we use, in the vertical direction, 672 equi-spaced grid points, with 256 equi-spaced grid points along both horizontal directions. The flow field in the horizontal directions is resolved in the Fourier space with 512 modes and along the vertical direction with a finite difference method (Cserepes *et al.* 1988). These numerical tricks permit an optimal resolution of the various thin and thick convective boundary layers that develop at the interfaces of the forth-constant viscosity horizontal layers. The model runs until a steady temperature is achieved. We studied several cases by varying the horizontal sizes of the computing box. A steady state was reached only when the small direction of the box, here 450 km along the y-direction, is significantly smaller than its large direction, here 750 km along the x-direction. This fact indicates that convection favours the development at depth of couples of rolls whose axis are parallel to the x- and y-directions and with a dimensionless length of 1.2 (750 km/640 km) and 0.7 (450 km/640 km), respectively (Cserepes *et al.* 1988). In our model, because of the viscosity decreases with height, the ascending flows concentrate and form plumes (Rabinowicz *et al.* 1990). The latter processes explain the unusual elliptic shape of the hot plumes heads (Fig. 8d). Conversely, dipping flows are sluggish and concentrate in thick vertical planes. This gives a polygonal shape to the return flow. Since the sizes of the polygons are not equal, these polygons do not have a purely hexagonal shape. Such a result is very specific to the present model: actually analogous 3-D experiments display purely hexagonal structures (Rabinowicz *et al.* 1990; Tackley 1993). It is very likely that this process results from the Rayleigh number of the experiment. In our model, across the 60-km thick highly viscous top layer, heat is essentially transported by conduction and the temperature step across that layer represents about 50 per cent of the potential temperature step across the entire height of the computing box. Besides, considering that the effective height of the convective layer is 580 km instead of 640 km, we see that the effective Rayleigh number of the 580 km high plume is $\sim$90 000 instead of 250 000. Constant viscosity convective experiments show a bifurcation from a bimodal to a smoked pattern beyond $\sim 5 \times 10^5$. These facts partly justify why the present structure of the flow is something intermediate between rectangles and hexagons.